



Istanbul
GEDİK
University
2651-5199

International Journal of
Engineering and
Natural Sciences

IJENS's

Vol:1 - Issue:1 - Year : 2018

Table of Contents:

Aim and Scope

Editorial Board and Advisory Board

Invariant Magnetic Vector Potential in the Mercury Based High-Temperature Superconductor and Its Prospective Technological Application

Güven Özdemir, Z. p. 1 – 5

Golden Ratio Discovered in Nonlinear Superconductor

Aslan Çataltepe, Ö.; Güven Özdemir, Z. and Onbaşı, Ü. p. 7 – 12

Failure Analysis of Jet Turbine Engine High Pressure Nozzle Material Made of Cobalt Based Super Alloy

Çoban, O.; Arslan, Ö. C. and Karahan, T. p. 13 – 20

Influence of Local Soil Conditions on the Structural Design and Associated Costs

İnce, H.; Toy, E. and Tolon, M. p. 21 – 25

The Experiment and Simulation Results of Speed Control of Permanent Magnet Synchronous Motor by Using Fuzzy Controller

Teker, A. and Kuyumcu, F.E. p. 27 – 31

Aim and Scope of IJENS's

International Journal of Engineering and Natural Sciences (IJENS) started its publishing life in December 2018. The aim of the journal is to serve researchers, engineers, scientists and all those who can benefit from it all over the world by providing theoretical and applicable knowledge in the field of engineering and natural sciences.

International Journal of Engineering and Natural Sciences (IJENS) covers a wide spectrum of research achievements. Thus, highly technological, creative and original research results, scientific reviews and short communication notes in a suitable balance of experimental, theoretical and computational aspects are considered for publication.

The publication language of the journal is English. Manuscripts previously published in another journal are not accepted.

The IJENS is free of charge and published three times a year. It allows authors to submit articles online and track their progress via its web interface.

Contact:

Istanbul Gedik University

Cumhuriyet Mahallesi İlkbahar Sokak No: 1-3-5

Yakacık 34876 Kartal, İstanbul, Turkey.

+90 - 216 444 5 438

International Journal of Engineering and Natural Sciences (IJENS's)

<https://www.gedik.edu.tr/akademik-birimler/akademik-yayinlar/mf-dergisi>

ijens@gedik.edu.tr

PUBLISHER

Zafer Utlü, Professor
Istanbul Gedik University

MANAGER

Gülperen Kordel
Istanbul Gedik University

PUBLICATION COORDINATOR

Nigar Dilşat Kanat
Istanbul Gedik University

EDITORIAL BOARD

Editor

Feriha Erfan Kuyumcu, Professor
Istanbul Gedik University

Associate Editors

Mert Tolon, Assistant Professor
Istanbul Gedik University

Serpil Boz, Assistant Professor
Istanbul Gedik University

Advisory Board

| | |
|--|----------------------------------|
| <i>Ahmet Zafer Öztürk</i> , Professor | Istanbul Gedik University |
| <i>Ahmet Topuz</i> , Professor | Istanbul Arel University |
| <i>Arif Hepbaşlı</i> , Professor | Yaşar University |
| <i>Arif Karabuga</i> , Lecturer | Istanbul Gedik University |
| <i>Auwal Dodo</i> , Ph.D. | Nottingham University |
| <i>Ayşen Demirören</i> , Professor | Istanbul Technical University |
| <i>Behiye Yüksel</i> , Associate Professor | Istanbul Gedik University |
| <i>Bora Alboyacı</i> , Associate Professor | Kocaeli University |
| <i>Devrim Aydın</i> , Assistant Professor | Eastern Mediterranean University |
| <i>Dilek Kurt</i> , Associate Professor | Istanbul Gedik University |
| <i>Fikret Tokan</i> , Associate Professor | Yıldız Technical University |
| <i>Gülşen Aydın Keskin</i> , Associate Professor | Kocaeli University |
| <i>Güner Arkun</i> , Professor | Istanbul Gedik University |
| <i>Gökhan Bulut</i> , Associate Professor | Istanbul Gedik University |
| <i>Hakan Yazıcı</i> , Associate Professor | Yıldız Technical University |
| <i>Halil Önder</i> , Professor | Istanbul Gedik University |
| <i>Haslet Ekşi Koçak</i> , Associate Professor | Istanbul Gedik University |
| <i>Mehmet Ali Baykal</i> , Professor | Istanbul Gedik University |
| <i>Hasila Jarimi</i> , Ph.D. | Nottingham University |
| <i>Hüseyin Günerhan</i> , Associate Professor | Ege University |

Murat Daniřman, Associate Professor Istanbul Gedik University
Mustafa Koçak, Associate Professor Gedik Holding
Nur Bekirođlu, Professor Yıldız Technical University
Nuran Yörükeren, Associate Professor Kocaeli University
Nurhan Türker Tokan, Associate Professor Yıldız Technical University
Nurettin Abut, Professor Kocaeli University
Özden Aslan Çataltepe, Associate Professor Istanbul Gedik University
Özgen Ümit Çolak Çakır, Professor Yıldız Technical University
Saffa Riffat, Professor Nottingham University
Serdar Küçük, Professor Kocaeli University
Sevinç İlhan Omurca, Associate Professor Kocaeli University
Siddık Sinan Keskin, Professor Marmara University
Sunullah Özbek, Professor Istanbul Gedik University
Tarık Baykara, Professor Dođuş University
Yanan Zhang, Ph.D. Nottingham University
Yate Ding, Ph.D. Nottingham University
Zafer Utlu, Professor Istanbul Gedik University
Zeynep Güven Özdemir, Associate Professor Yıldız Technical University

Invariant Magnetic Vector Potential in the Mercury Based High-Temperature Superconductor and Its Prospective Technological Application

Z. Güven Özdemir¹

¹ Department of Physics, Yildiz Technical University, Davutpaşa, 34010, Istanbul, Turkey.
zgozdemir@gmail.com; zguven@yildiz.edu.tr

Received: 21.11.2018 Accepted: 17.12.2018

Abstract: Magnetic vector potential, A has great importance in various superconducting phenomena such as Aharonov-Bohm effect, Josephson effect, SQUID applications etc. due to the fact that A is directly related to the phase difference in the superconducting system. In this work, magnetic vector potential value has been calculated numerically for the optimally oxygen doped $\text{HgBa}_2\text{Ca}_2\text{Cu}_3\text{O}_{8+x}$ mercury cuprate superconductor via interlayer theory at low temperatures by using magnetization versus applied magnetic field data. It has been surprisingly determined that regardless of the temperature variation; the quantity of magnetic vector potential remains unchanged. In this context, it has been determined that magnetic vector potential is an invariant parameter of the system investigated. Moreover, momentum conserving interlayer tunneling i.e. coupling between superconducting copper oxide layers for a low-temperature interval of 3K-5K has been proved for the first time. Hence, invariant magnetic vector potential corresponds to the concept of the constant phase difference. Ultimately, this work gives a reliable method for deciding about working temperature interval for technologists who want to design an intrinsic phase detector which has the property of constant phase difference.

Keywords: Invariant magnetic vector potential, mercury cuprates, momentum conserving interlayer theory, phase.

1. INTRODUCTION

From a theoretical point of view, magnetic vector potential, A has great importance as a physical quantity in the unified field theories of fundamental forces which combine the electromagnetic force, weak and strong nuclear forces and gravity. As is known, vector potential is the most known gauge field of electromagnetism. Observation of the Aharonov-Bohm (AB) effect also enables us to comprehend the derivation of a gauge field physically [1]. The motion of a charged particle can sometimes be affected by electromagnetic fields in regions that the particle never enters. This phenomenon is known as the AB effect which is a non-local effect. In this effect, a physical object moves along a closed loop through a gauge field free region and hence it experiences some physical changes [2]. Due to the existence of a magnetic vector potential, in AB effect a charged particle exhibits a phase shift even if there is no magnetic field [3]. Moreover, quantization of magnetic flux is closely related to AB effect and superconductors constitute a natural frame of reference for observation of magnetic flux quantum [4, 5]. In this context, there have been various superconducting applications whose working

principle is based on magnetic vector potential i.e. phase such as SQUID etc. Furthermore, achieving non-varying magnetic vector potential i.e. constant phase difference has a crucial role in various technological applications which are based on phase locking. As is known, there have been several works on cryogenic phase detector which is based on Josephson junction and superconducting flux flow oscillator for phase locking with Nb [6-9].

In addition to this technological importance of magnetic vector potential, achieving non-varying (invariant) magnetic vector potential has a crucial role for theoretical works focused on the explanation of electrical conductivity mechanism in cuprate superconductors. So that verification of the invariant magnetic vector potential experimentally in cuprate superconductors enables us to understand the momentum conserving interlayer coupling which is responsible for electrical conductivity in cuprate superconductors that was proposed by P. W. Anderson et al. in the mid-1990s [10,11].

In this context, due to reasons mentioned above, determining of magnetic vector potential has vital importance for advanced technological applications as well as theoretical works.

In this work, a numeric calculation of magnetic vector potential of the optimal oxygen doped mercury-based copper oxide layered high-temperature superconductor has been realized by using magnetization versus magnetic field hysteresis curves obtained by Superconducting Quantum Interference Device (SQUID).

Mercury cuprates have the highest Meissner critical transition temperature of 140K at normal atmospheric pressure, high critical current densities in the order of 10^{12} [A/m²]. Moreover, in our previous works, it has been determined that the mercury-based high-temperature superconducting system is a reliable frame of reference for observing some symmetry breakings. As was previously reported that one-dimensional global gauge symmetry U (1), time reversal symmetry, T and electro-weak symmetry are broken in a mercury cuprate superconductor. Moreover, mercury cuprate exhibits some relativistic effects such as shifting of plasma frequency from microwave to infrared that corresponds to a gravitational redshift in general relativity and Paramagnetic Meissner effect which origins from spin-orbit coupling process in the system [12-15]. From this point of view, determination of magnetic vector potential, A of the mercury cuprate has crucial importance.

2. THEORETICAL

Magnetic vector potential has been investigated in the context of interlayer theory for the optimal oxygen doped HgBa₂Ca₂Cu₃O_{8+x} (Hg-1223) superconductors since the interlayer theory had already been confirmed in three dimensions at low temperatures in our previous works [16-18].

The interlayer theory explains the superconductivity in the copper oxide layered superconductors in terms of the occurrence of crossover from two-dimensional to three-dimensional coherent electron pair transport [18]. The realization of the three-dimensional coherent electron pair transport is achieved by the Josephson or Lawrence-Doniach-like coupling between the superconducting copper oxide layers [19,20]. Accordingly, the Josephson coupling energy is to be equal to superconducting condensation energy so that the superconducting system exhibits perfect coupling along the c-axis [19]. For low temperatures ($T \ll T_c$) free energy of superconductor, F can be taken as superconducting condensation energy, E_b . In this respect, critical current density, J_c is written as

$$J_c = c \frac{\partial F}{\partial A} \approx c \frac{\partial E_b^0}{\partial A} \quad (1)$$

Since the superconducting condensation energy almost comes from Josephson coupling between copper oxide layers, E_b is written as Josephson coupling energy form

$$E_b = -E_b^0 \cos \theta \quad (2)$$

where E_b^0 and θ are the amplitude of superconducting condensation energy and the phase difference between superconducting layers, respectively [19].

The phase difference is defined in terms of the magnetic vector potential, A by Eq. (3)

$$\theta = \frac{2es}{\hbar c} A \quad (3)$$

where s is the average distance between copper oxide layers, e is the charge of an electron, c is the velocity of light and \hbar is the Planck's constant divided by 2π . For relatively small phase differences, the critical current density is determined as Eq. (4) by using Eqs. (1), (2) and (3).

$$A = \frac{J_c \hbar^2 c^2}{4cE_b^0 e^2 s^2} \quad (4)$$

The c-axis penetration depth i.e Josephson penetration depth is also written by London equation [19]. The Josephson penetration depth represents the penetration of the magnetic field induced by the supercurrent flow in the superconductor.

$$\lambda_c = \sqrt{\frac{c}{4\pi} \frac{A}{J_c}} = \frac{\hbar c}{4es} \frac{1}{\sqrt{\pi E_b^0}} \quad (5)$$

3. RESULTS

In our one of the previous works, the interlayer theory had already been confirmed for the optimal oxygen doped HgBa₂Ca₂Cu₃O_{8+x} (Hg-1223) mercury cuprates by determining the equality of Josephson coupling energy and superconducting condensation energy at the temperature interval of 3K-7K [16]. Due to this reason, this work has been focused on this low-temperature interval.

Critical current densities and c-axis penetration depths of the optimally oxygen doped Hg-1223 superconductors, which are accepted as the key parameters for calculation of magnetic vector potential, had already been calculated for 4,2K, 27K and 77K temperatures by Bean critical state and Lawrence - Doniach model, respectively [16-18]. The critical current density has been calculated according to Eq. (6).

$$J_c = 120\pi \frac{\Delta M}{t} \quad (6)$$

Where ΔM is the magnetization difference between the increasing and decreasing field branches and t is the average grain size of the sample.

These parameters had been determined via

magnetization versus applied magnetic field ($M-H$) dynamic hysteresis curves obtained by very sensitive quantum design SQUID magnetometer, model MPMS-5S. Related $M-H$ dynamic hysteresis curves are given in Fig. 1. According to related data, critical current densities and c -axis penetration depths of the optimally oxygen doped Hg-1223 superconductors at the temperature interval of 3K-7K has been determined by fitting functions which are given Eqs. (7) and (8), respectively. The results are also listed in Table 1.

$$J_c = 1.398 \times 10^{12} \exp\left(-\frac{T}{12.262}\right) + 7.379 \times 10^9 \quad (\text{with } R^2 = 1) \quad (7)$$

$$\lambda_j = 0.499 + 0.016T + 6.717 \times 10^{-4} T^2 \quad (\text{with } R^2 = 1) \quad (8)$$

According to Eq. (5), the amplitude of the superconducting condensation energy, has been calculated. By using Eq. (4) and values in Table 1, magnetic vector potential A has been determined.

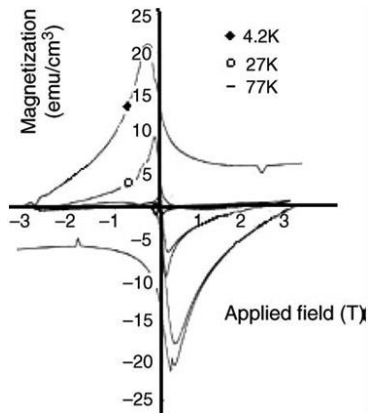


Figure 1. Magnetization versus applied magnetic field ($M-H$) for the optimally oxygen doped Hg-1223 superconductors at 4.2, 27 and 77 K [18].

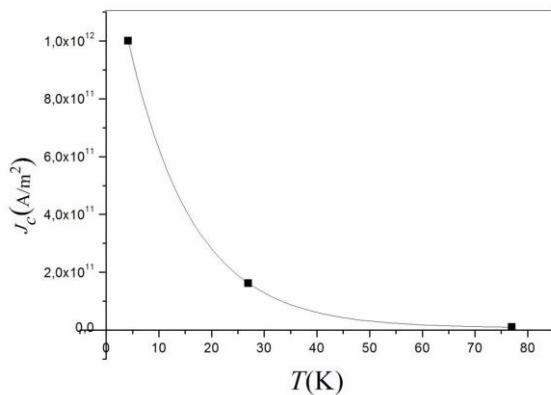


Figure 2. Critical current density versus temperature for the optimally O_2 doped Hg-1223 superconductor.

As shown in Table 1, regardless of the temperature variation, magnetic vector potential has the same value for

3K-5K temperature interval. From this point of view, magnetic vector potential is considered as an invariant parameter of the system for this temperature interval. So that the phase difference between superconducting layers in the system is also constant. The constant i.e. invariant phase difference for temperature interval of 3K-5K has been calculated by Eq. (3) in terms of magnetic vector potential:

$$\theta = 1,125.10^{-10} (m/s)^{-1}$$

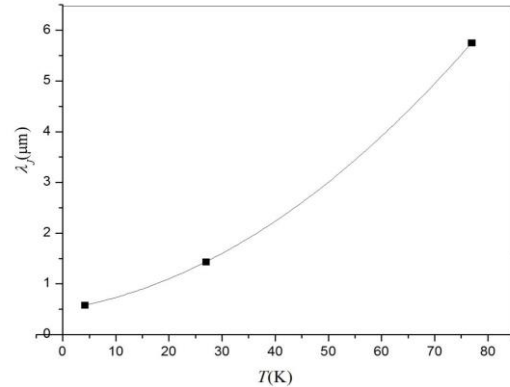


Figure 3. Josephson penetration depth versus temperature for the optimally O_2 doped Hg-1223 superconductor.

Table 1. Josephson penetration depth, critical current density, the amplitude of superconducting condensation energy and magnetic vector potential values for the optimally oxygen doped Hg-1223 superconductor at low temperatures.

| $T(K)$ | $J_c(A/m^2)$ | $\lambda_j(\mu m)$ | $E_b^0 (J/m^3)$ | $A(Vs/m)$ |
|--------|-----------------------|--------------------|-----------------------|-----------------------|
| 3 | 1.10×10^{12} | 0.55 | 4.05×10^{15} | 1.41×10^{-8} |
| 4 | 1.02×10^{12} | 0.58 | 3.77×10^{15} | 1.41×10^{-8} |
| 5 | 0.94×10^{12} | 0.59 | 3.48×10^{15} | 1.41×10^{-8} |
| 6 | 0.86×10^{12} | 0.62 | 3.22×10^{15} | 1.39×10^{-8} |
| 7 | 0.80×10^{12} | 0.65 | 2.97×10^{15} | 1.40×10^{-8} |

According to Eq. (3), the unit of the phase difference between superconducting layers in the system corresponds to the inverse of the unit of velocity. Since magnetic vector potential is related to the phase difference, which is interpreted as an inverse of velocity in the system, the magnetic vector potential is considered as “electromagnetic momentum” per charge. Traditionally, in order to obtain an “invariant momentum” by means of “conserved momentum”, the electromagnetic momentum of qA is added to linear momentum mv as shown in Eq. (6)

$$p = mv + qA \quad (6)$$

where m is mass, v is the velocity of the charged particle, and q is the charge. So that the different choices for vector potential A cause different generalized momentums and some choices of A result in non-conserved generalized

momentum [21]. In this context, choices for A have great importance to get conserved momentum which is related to homogeneous space that is invariant under translational symmetry.

On the other hand, since invariant magnetic vector potential leads to conserved momentum; it is natural to conclude that superconducting copper oxide layers in mercury cuprates are coupled by Josephson tunneling mechanism with interlayer momentum conservation. In this context, the concept of momentum conserving interlayer coupling has been numerically proved for the first time by using some electrodynamics parameters that are derived from a magnetization versus applied magnetic field experimental data.

Moreover, achieving invariant magnetic vector potential i.e. constant phase difference has also great importance for superconducting technological applications related to phase locking. In this point of view, if one works with the optimally oxygen doped mercury cuprates at the temperature interval of 3K-5K, since the phase difference is constant, any kind of minor effect that makes a change of the phase of the system could be detected by the suitable measurement system.

4. CONCLUSIONS

In this work, it has been numerically proved that magnetic vector potential acts as an invariant gauge field in the mercury-based high-temperature superconductors at low temperatures. This result has important theoretical and technological consequences. From a theoretical point of view, it has been understood that mercury cuprates realize Josephson coupling with the conserved momentum by introducing constant magnetic vector potential intrinsically. According to the technological point of view, this work gives a reliable working temperature interval of 3K-5K to technologists who want to design a phase detector with mercury cuprates. Since both bulk mercury cuprates consist of intrinsic Josephson junction array that displays three dimensional Josephson plasma resonance and exhibits invariant phase difference for a particular temperature interval, the optimal oxygen doped $\text{HgBa}_2\text{Ca}_2\text{Cu}_3\text{O}_{8+x}$ mercury cuprate superconductors can be proposed as the promising candidate for development of cryogenic phase detector and superconducting integrated receiver.

ACKNOWLEDGMENT

I would like to thank Prof. Dr. Ü. Onbaşlı for her valuable discussions and experimental contributions on magnetic vector potential.

REFERENCES

- [1] T.T. Wu and C.N. Yang, "Concept of nonintegrable phase factors and global formulation of gauge fields", *Phys. Rev. D*, vol. 12, pp. 3845-3857, 1975.
- [2] H. Lyre, "Aharonov—Bohm Effect", in: *Compendium of Quantum Physics*, D. Greenberger, K. Hentschel, F. Weinert F. (Eds.), Springer, Berlin, Heidelberg 2009, pp. 1-3.
- [3] Y. Aharonov and D. Bohm, "Significance of electromagnetic potentials in the quantum theory", *Phys. Rev.*, vol. 115 pp. 485-491, 1959.
- [4] R. Doll and M. Nabauer, "Experimental proof of magnetic flux quantization in a superconducting ring", *Phys. Rev. Lett.*, vol. 7, pp. 51-52, 1961.
- [5] B.S. Deaver and W.M. Fairbank, "Experimental evidence for quantized flux in superconducting cylinders", *Phys. Rev. Lett.*, vol. 7, pp. 43-46, 1961.
- [6] A.V. Khudchenko, V.P. Koshelets, P.N. Dmitriev, A.B. Ermakov, P.A. Yagoubov, and O.M. Pylypenko, "Cryogenic phase detector for the superconducting integrated receiver", *IEEE Trans. Appl. Supercond.* vol. 17, pp. 605-608, 2007.
- [7] P.V. Koshelets, S.V. Shitov, A.B. Ermakov, L.V. Filippenko, O.V. Koryukin, A.V. Khudchenko, M.Y. Torgashin, P.A. Yagoubov, R.W.M. Hoogeveen, and O.M. Pylypenko, "Superconducting integrated receiver for TELIS", *IEEE. Trans. Appl. Supercond.*, vol. 15, pp. 960-963, 2005.
- [8] V.P. Koshelets, S.V. Shitov, P.N. Dmitriev, A.B. Ermakov, L.V. Filippenko, V.V. Khodos, V.L. Vaks, A.M. Baryshev, P.R. Wesseliuss, and J. Mygind, "Towards a phase-locked superconducting integrated receiver: Prospects and limitations", *Physica C*, vol. 367, pp. 249-255, 2002.
- [9] V.P. Koshelets and S.V. Shitov, "Integrated superconducting receivers", *Superconductor Science and Technology*, vol. 13, pp. R53-R69, 2000.
- [10] S. Chakravarty and P.W. Anderson, "Interlayer Josephson tunneling and breakdown of Fermi liquids", *Phys. Rev. Lett.*, vol. 72, pp. 3859-3862, 1994.
- [11] S. Chakravarty, A. Sudbø, and P.W. Anderson, "Strong interlayer tunneling and gap anisotropy in high temperature superconductors", *Science*, vol. 261, pp. 337-340, 1993.
- [12] Ö. Aslan Çataltepe, "Mercury cuprates bring symmetry breaking of the Universe to laboratory", in: *Lifetime of the Waves From Nano To Solitons In My Life*, Ü. Onbaşlı, Ed., Kerela, India: Transworld Research Network, 2012, pp. 215-243. (Available from http://www.tnres.com/ebook/uploads/onbaslicontent/T_1350723744_5%20Onbasli.pdf)
- [13] Ö. Aslan Çataltepe, "Some chaotic points in cuprate superconductors", in: *Superconductor*, A.M. Luiz, Ed., India: Sciy Company, 2010, pp. 273-290. (Available from <http://www.intechopen.com/articles/show/title/some-chaotic-points-in-cuprate-superconductors>)
- [14] Ü. Onbaşlı, Z. Güven Özdemir, "Superconductors and quantum gravity", in: *Superconductor*, A.M. Luiz, Ed., India: Sciy Company, 2010, pp. 291-310. (Available from <http://www.intechopen.com/articles/show/title/superconductors-and-quantum-gravity>)
- [15] Ü. Onbaşlı, Z. Güven Özdemir, and Ö. Aslan, "Symmetry breakings and topological solitons in mercury based d-wave Superconductors", *Chaos Solitons Fractals*, vol. 42, pp. 1980-1989, 2009.
- [16] Z. Güven Özdemir, Ö. Aslan, and Ü. Onbaşlı, "Terahertz oscillations in mercury cuprate Superconductors", *Pramana-J. Phys.*, vol. 73, pp. 755-763, 2009.
- [17] Z. Güven Özdemir, Ö. Aslan, and Ü. Onbaşlı, "Calculation of microwave plasma oscillations in high temperature Superconductors", in: *The 7th International Conference on Vibration Problems (ICOVP 2005) Springer Proceedings in Physics 111*, E. İnan, E. Kırış (Eds.), Dordrecht, The Netherlands: Springer, 2007, pp. 377-382.
- [18] Z. Güven Özdemir, Ö. Aslan, and Ü. Onbaşlı, "Determination of c-axis electrodynamics parameters of mercury cuprates", *J. Phys. Chem. Solids*, vo. 67, pp. 453-456, 2006.

- [19] P.W. Anderson, "c-Axis electrostatics as evidence for the interlayer theory of high-temperature superconductivity", *Science*, vol. 279, pp. 1196-1198, 1998.
- [20] W.E. Lawrence and S. Doniach, "Theory of layered structure superconductors", in: *Proceedings of the 12th International Conference on Low Temperature Physics*, E. Kanda (Ed.), Kyoto: Kanda Academic Press of Japan, 1971, pp. 361-362.
- [21] M.D. Semon and J.R. Taylor, "Thoughts on the magnetic vector potential", *Am. J. Phys.*, vol. 164, pp. 1361-1369, 1996.

Golden Ratio Discovered in Nonlinear Superconductor

Özden Aslan Çataltepe¹, Zeynep Güven Özdemir² and Ülker Onbaşlı³

¹ Faculty of Engineering, İstanbul Gedik University, Kartal, 34876, İstanbul, Turkey.

² Department of Physics, Yıldız Technical University, Davutpaşa, 34010, İstanbul, Turkey.

³ Department of Physics, Marmara University, Göztepe, 34722, İstanbul, Turkey.

ozden.aslan@gedik.edu.tr, zguven@yildiz.edu.tr

Received: 23.11.2018 Accepted: 19.12.2018

Abstract: Mercury based high temperature superconductor as a nonlinear dynamical system constitutes a natural laboratory for searching quantum chaotic transitions. In our previous works, these chaotic transitions had been expressed in details and mathematically proved by determination of negative Schwarzian derivative. In this work, we have focused on the net effective mass of the quasi particles, m^* at the vicinity of absolute zero temperature and the mass of the double helix quantum wave i.e. topological Segah solitons. The net effective mass of the quasi particles as the function of the phase of the superconducting system had already been determined in our previous works by using an advanced differential method that is based on the magnetic data obtained by SQUID (Superconducting Quantum Interference Device) measurements. The mass of the double helix quantum wave, whose wave length coincides with ultraviolet region of the electromagnetic spectrum, m_{uv} , has also been calculated with the wave length of the solitons in relativistic manner. Since we have already proved the three dimensional resonance at low temperatures for the mercury cuprates, the determination of the ratio of these masses at the vicinity of absolute zero would be a promising method for searching the properties of resonance. Hence, we have determined the resonance state which appears as the golden ratio in m_{uv}/m^* values for the distances $x=0.23\mu\text{m}$ and $x=2,361\mu\text{m}$ at absolute zero temperature for the optimally and over oxygen doped mercury cuprate superconducting nonlinear condensed matter system, respectively.

Keywords: Golden ratio, net effective mass, solitons' mass, mercury cuprate, nonlinear condensed matter system.

1. INTRODUCTION

Everything in nature exists with an intrinsic measure and the evidence of this fact is realized by means of the fundamental called as golden ratio. Golden ratio is a universal irrational mathematical constant and appears in both macroscopic and microscopic scales, such as the design of the Egyptians' Pyramids and architecture, in music, in the physical proportion of the human body, the DNA molecule and many other aspects of life and that of the Universe. Moreover, in order to achieve harmony, balance and beauty, mankind also uses the Nature's golden ratio in their own creations of art, architecture, colors, design, and music [1]. Furthermore, in January 2010, the golden ratio has been discovered in cobalt niobate at the quantum physical level. When a strong magnetic field has been applied to cobalt niobate, it enters a "quantum critical state" and hence the spin dynamics of the system shows a fine structure with two sharp modes at low energies. Golden ratio has been determined in the ratio of the first two

frequencies of the mentioned modes [2]. In this context, it is natural to think that the quantum world has also its own special order which is described by the golden ratio, as well. From this point of view, this work is devoted to investigate the special order to describe the nature of the high temperature superconductors which is mainly based on harmony and resonance. Moreover, superconductors, which have a crucial role in the establishment of nonlinear quantum theory due to observation of some macroscopic quantum effects, also constitute a natural frame of reference to observe the quantum chaotic transitions which emanate themselves as spontaneous symmetry breakings due to nonlinear interactions within the system [3, 4]. The concept of symmetry breakings in superconductors especially in mercury based high temperature superconductors had been discussed by means of chaotic behavior (i.e. chaotic transitions) in details in our previous works [5-8]. Furthermore, solitons, which are accepted as a universal concept in nonlinear science, had also been previously predicted in the mercury based high temperature

superconductors [5]. Due to these reasons mentioned above, determination of the special order (i.e. golden ratio) in the resonance state of the nonlinear condensed matter system may give an insight for both experimentalists and theoreticians.

In this work, the golden ratio has been investigated for both the optimally and over oxygen doped high T_c copper oxide layered mercury cuprates in the context of the net effective mass of the quasi-particles and solitons' mass.

The net effective mass of the quasi-particles has already been calculated by "Ongüas Equation" which we have derived in our previous works [9-11]. The derivation of the Ongüas equation is based on an advanced analogy between the supercurrent density and the phase of the superconducting order parameter. The Ongüas Equation also enables us to determine the net effective mass of the quasi-particles by using the magnetization versus applied magnetic field experimental data obtained by high sensitive superconducting quantum interference device (SQUID). Moreover, the net effective mass of the quasi-particles is related to the occurrence of the Higgs mechanism in the superconducting state [12, 13].

Mass of solitons i.e. topological solitons so called Segâh solitons in the mercury cuprates has been calculated for the first time in this work. Topological Segâh soliton has already been defined in three dimensional quantum mechanical unit cell of the d-wave $\text{HgBa}_2\text{Ca}_2\text{Cu}_3\text{O}_{8+x}$ (Hg-1223) superconductor in our previous works [5,14].

According to our calculations, we have theoretically discovered that m_{uv}/m^* values approach Golden ratio for both the optimally and over oxygen doped mercury cuprate superconductors for different distances in micrometer at the vicinity of absolute zero temperature. As is accepted that absolute zero temperature is the most appropriate temperature for searching the golden ratio since it represents the lowest quantum state. Moreover, it is a remarkable point that golden ratio, which is the signature of intrinsic special order appeared in the nonlinear system by means of the superconductor, is determined within micrometer scale, that is comparable with Josephson penetration depth. However, the special order appeared in micrometer interval for the optimally oxygen doped Hg-1223 superconductor has been determined ten times smaller than that of the over doped sample.

2. THEORETICAL

The derivation of the net effective mass of the quasi-particles with respect to temperature has already been expressed in our previous works [9-11]. Since calculation of the net effective mass is one of the essential steps of this work, the derivation process is expressed as follows.

The term of "net effective mass" represents the total output of the effective masses in the layered structured superconducting system since the mercury cuprate superconductors exhibit spatial (three dimensional)

resonance due to occurrence of the intrinsic Josephson effects between superconducting copper oxide layers [15,16]. The net effective mass of the quasi-particles, m^* , has been calculated by the Ongüas Equation which constitutes a relationship between the net effective mass and the phase, φ of the superconducting order parameter, Ψ . The only variable phase, φ is accepted as the most important parameter of this quantum system. Moreover, due to the intrinsic Josephson effect in mercury cuprates, for application of low magnetic fields (lower than H_{c1} at which all of the magnetic flux is totally expelled from the superconductor), the phase in the junctions is written as a function of distance x ,

$$\varphi(x) = \varphi_o \exp\left(-\frac{x}{\lambda_j}\right) \quad (1)$$

where φ_o is phase value at $x=0$ and λ_j is Josephson penetration depth [17,18].

The Josephson penetration depth, λ_j describes the penetration of the magnetic field induced by the super current flow in the superconductor [15, 19].

The magnetic field at any points of the intrinsic Josephson junction mentioned, $H(x)$ and the supercurrent density, J_s are proportional to the first and second derivation of the phase with respect to distance, respectively [17,18]. The first derivative of the velocity with respect to wave vector is proportional to the reverse of the effective mass which is well known in condensed matter physics. Due to the fact that supercurrent density depends on the velocity of the quasi-particles, in order to obtain the net effective mass of the quasi-particles, the first derivative of the J_s with respect to distance has been taken. In this context, the net effective mass formula "Ongüas Equation" has been achieved [9-11].

$$\frac{dJ_s}{dx} = \frac{1}{\varphi_o m^*} = \frac{c\Phi_o}{8\pi^2 d} \left(-\frac{1}{\lambda_j}\right)^3 \exp\left(-\frac{x}{\lambda_j}\right) \quad (2)$$

where c is the speed of light, Φ_o is the magnetic flux quantum and d is the average distance between the superconducting copper oxide layers.

"Ongüas Equation" also confirms the P.W. Anderson's suggestion that the effective mass is expected to scale like the reverse of the supercurrent density [20].

3. EXPERIMENTAL WORKS and RESULTS

In this section, the variation of the net effective mass of the quasi-particles (Cooper pairs) with distance and calculation of solitons' i.e. double helix quantum wave's mass appeared in the quantum mechanical unit cell of the superconducting system have been investigated at the

vicinity of the absolute zero temperature for both the optimally and over oxygen doped mercury cuprate superconductors, Hg-1223.

3.1. Net Effective Mass of the Quasi-Particles

The net effective mass values of the quasi-particles at zero Kelvin have been calculated by Ongüas Equation for various distance values varying from zero to λ_j . The required electrodynamics parameter of the Josephson penetration depths have already been calculated in our previous works [15,16]. In the calculation process of λ_j , the critical current densities have been calculated by Bean critical state model via the magnetization versus magnetic field data performed by SQUID [15]. All calculations have been made at or below the lower critical field magnetic field of H_{c1} . So that there is no need to consider any vortex contribution since all magnetic field applied is totally expelled from the superconductor. The related $\lambda_j = f(T)$ functions for the optimally and over oxygen doped Hg-1223 superconductors are given in Figure 1 (a) and (b), respectively.

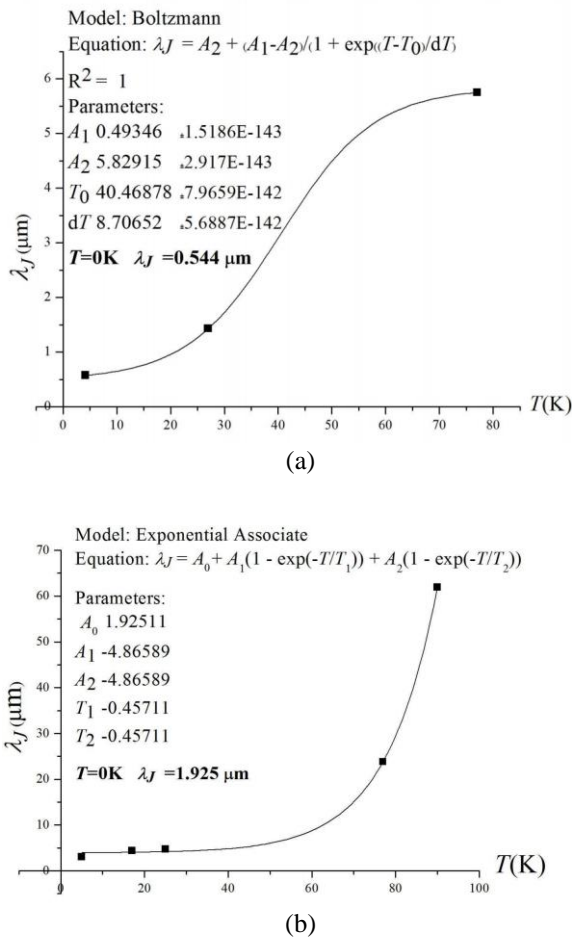


Figure 1. The Josephson penetration depth versus temperature graphics and their fitting functions for (a) the

optimally and (b) over oxygen doped Hg-1223 superconductor.

The Josephson penetration depth values at zero Kelvin have been determined by the fitting functions of λ_j in Figure 1 for the optimally and over oxygen doped Hg-1223 superconductors, respectively. The related Josephson penetration depths are given in Table 1.

Table 1. The Josephson penetration depth values at the absolute zero temperature for the optimally and over oxygen doped Hg-1223 superconductors.

| Hg-1223 mercury cuprate material | λ_j (μm) at $T=0\text{K}$ |
|----------------------------------|--|
| Optimally O ₂ doped | 0.544 |
| Over O ₂ doped | 1.925 |

According to Table 1 it has been determined that the magnitude of the Josephson penetration depth value of over doped sample at absolute zero increases four times with respect to that of the optimally doped samples.

The net effective mass of the quasi-particles at zero Kelvin for different distance values have been calculated by Eq. (2). The related data have been given in Table 2.

3.2. Double Helix Quantum Wave's Mass

The double helix quantum wave, DHQW, is a natural and characteristic consequence of the d-wave symmetry in the copper oxide layers of cuprate superconductors, which is represented as a four-leaf clover. As was previously explained in details in our previous works, the three dimensional double helix quantum structure can be attributed to the solitons as the time period of the wave is taken infinite in the phase space. We have called this intrinsic quantum waves as "Segâh Solitons" which refers to the topological solitons [5, 14]. Determination of the topological solitons in the mercury based superconductors enable us to discuss the system as a nonlinear condensed matter media, as well.

The topological solitons are considered as the intrinsic property of the superconducting copper oxide systems. The frequency of the DHQW that corresponds to ultraviolet (u.v.) region of electromagnetic spectrum has been calculated from Figure 2.

The average distance between copper oxide layers is $d = 7.887 \times 10^{-10}$ m determined by XRD measurements. According to Figure 2, the wave length of DHQW is calculated as follows. d-wave symmetry schematically represented in the copper oxide layers as a four-leaf clover completes 360° within seven layers.

$$\lambda = 7d = 5.5209 \times 10^{-9} \text{ m}$$

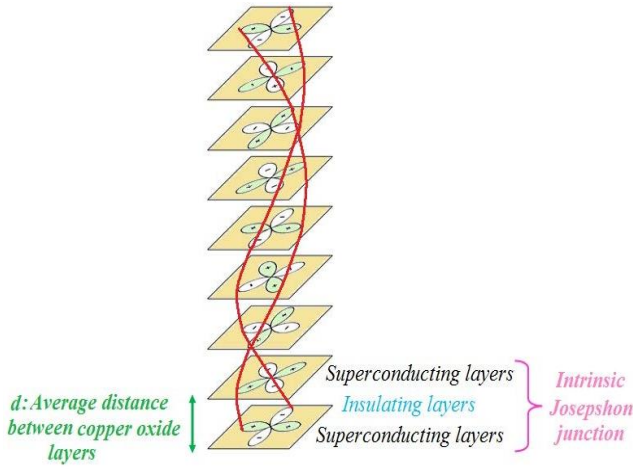


Figure 2. The schematic illustration of the DHQW (red line) as a topological solitons in the mercury cuprate superconductors [5,14]. There is a 45° phase difference between each superconducting copper oxide layer [21].

The wave length of DHQW is independent from the oxygen content, since we have determined that the parameter “ d ” is very slightly affected by oxygen annealing process. In this context, one has the right to take the same wave length value for both the optimally and over oxygen doped samples [7].

In order to calculate topological solitons’ mass, a relativistic approach has been applied. As is known that the superconducting system mentioned is considered as a relativistic frame of reference due to exhibition of two characteristics relativistic effects which are summarized as follows:

Mercury cuprate superconductors can be accepted as the most convenient and reliable candidate frame of reference to extend the comprehension to understand the emerging procedure of mass since they display electroweak symmetry breaking [5, 10, 14]. Moreover, plasma frequency of Hg-1223 system shifts from microwave to infrared. Both the occurrence of the electroweak symmetry breaking and the frequency shifting phenomenon in the mercury cuprate system enable us to deal with solitons’ mass in terms of relativistic manner [10, 14]. Solitons’ mass is abbreviated as m_{uv} since its frequency coincides with ultraviolet region of electromagnetic spectrum. In this context,

$$m_{uv} = h/\lambda c = 3.997 \times 10^{-34} \text{ kg}$$

where h is the Planck constant.

Both m_{uv} and m^* which are the intrinsic masses, define the wave and particle properties of the system, respectively. Since m_{uv} is related to d-wave symmetry character of the Hg-1223, m_{uv} value is independent from the temperature and oxygen content in the superconducting state. In this context, we have taken the same m_{uv} mass value belonging

to DHQW for the optimally and over doped Hg-1223 superconductors. Since we have already proved the three dimensional resonance for low temperatures in our previous works [15, 16, 22], it is convenient to take the ratio of the masses at the vicinity of absolute zero for searching the properties of the resonance in terms of mass.

According to data in Table 2, the ratio of m_{uv}/m^* versus distance x graphics has been given in Figure 3 for the optimally and over oxygen doped Hg-1223 superconducting materials, respectively.

Table 2. The ratios of m_{uv} and m^* at different distances for the optimally and over oxygen doped mercury cuprates at absolute zero temperature. The data written in bold has been obtained by fitting functions given in Figure 3.

| The optimally oxygen doped Hg-1223 | | |
|------------------------------------|-------------------------|---|
| $x(\mu\text{m})$ | $m^*(\text{kg})$ | m_{uv}/m^* |
| 0 | $1,618 \times 10^{-20}$ | 2.469×10^{-14} |
| 0.1 | $1,945 \times 10^{-20}$ | 2.055×10^{-14} |
| 0.2 | $2,337 \times 10^{-20}$ | 1.710×10^{-14} |
| 0.23 | | 1.618×10^{-14} |
| 0.3 | $2,808 \times 10^{-20}$ | 1.423×10^{-14} |
| 0.4 | $3,375 \times 10^{-20}$ | 1.184×10^{-14} |
| 0.5 | $4,057 \times 10^{-20}$ | 0.985×10^{-14} |
| 0.6 | $4,880 \times 10^{-20}$ | 0.819×10^{-14} |
| The over oxygen doped Hg-1223 | | |
| $x(\mu\text{m})$ | $m^*(\text{kg})$ | m_{uv}/m^* |
| 0 | $7,173 \times 10^{-19}$ | 5.572×10^{-16} |
| 0.5 | $9,297 \times 10^{-19}$ | 4.299×10^{-16} |
| 1 | $1,205 \times 10^{-18}$ | 3.316×10^{-16} |
| 2.379 | | 1.618×10^{-16} |
| 1.5 | $1,563 \times 10^{-18}$ | 2.557×10^{-16} |
| 2 | $2,026 \times 10^{-18}$ | 1.972×10^{-16} |
| 3 | $3,410 \times 10^{-18}$ | 1.172×10^{-16} |
| 4 | $5,734 \times 10^{-18}$ | 0.697×10^{-16} |

According to the exponential decay fitting functions obtained by Origin Lab 8.0 in Figure 3, it has been determined that for $x=0.23\mu\text{m}$ and $x=2.361\mu\text{m}$ at $T=0\text{K}$, the magnitude of the ratio of m_{uv}/m^* approaches to the golden ratio for the optimally and over oxygen doped Hg-1223 superconductors, respectively. As is known, the magnitude of the ratios has the great importance to decide about the golden ratio since multiplication factor (10^{-14} and 10^{-16}) depends on the frame of reference investigated. As an

example, by dealing with the superconductivity in neutron stars the multiplication factor is completely different than that of a superconductor investigated in a laboratory.

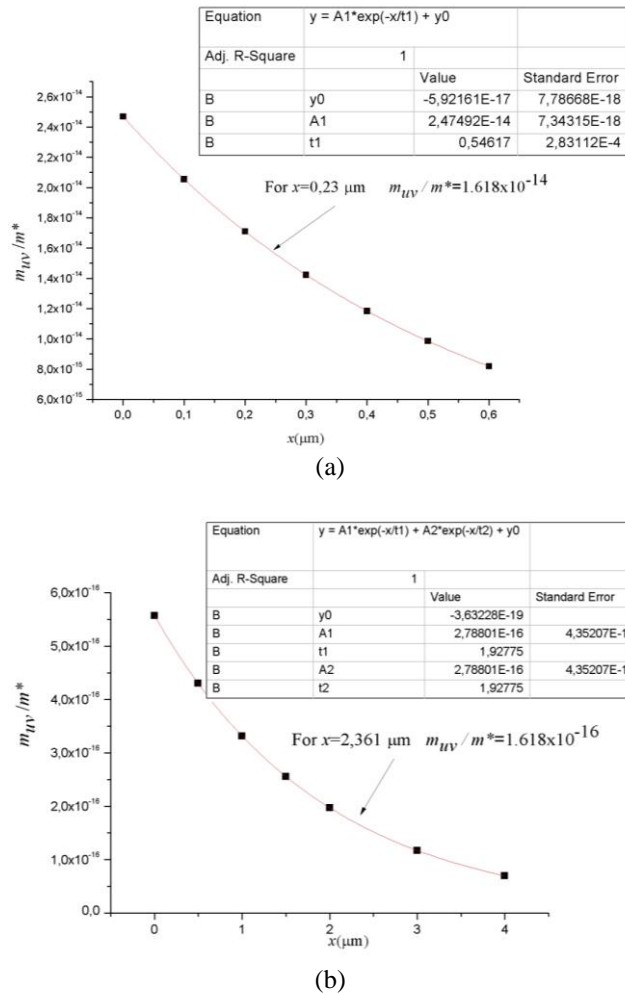


Figure 3. The ratio of m_{HV}/m^* versus distance x for (a) the optimally and (b) over oxygen doped Hg-1223 superconductor. According to the fitting functions determined by Origin Lab, golden ratio emanates itself at $x=0.23 \mu\text{m}$ and $x=2.361 \mu\text{m}$, respectively

4. DISCUSSION and CONCLUSION

In this work, the topological soliton's mass, which is of the intrinsic properties of the superconducting copper oxide layered systems, has been calculated for the first time. It has been determined that the DHQW's mass is 10^{-3} times lighter than electron's mass. Also, we have found that the ratio of solitons' mass to net effective mass of the quasi-particles i.e. the magnitude of m_{HV}/m^* approaches to the universal number so called as the golden ratio for Hg-1223 nonlinear superconducting system. The oxygen content of the system affects the distance parameter of x at which the golden ratio is observed. x values are different from London penetration depth of the samples. While x value is bigger than λ_j value

for over doped sample, it is lower than that for optimum doped. In the study, it has been interpreted that observing of the golden ratio in the ratio of masses for the nonlinear system by means of superconducting sample is an intrinsic property of the system.

Ultimately, determining the golden ratio in superconducting systems reveals the intrinsic quantum order that leads to develop the resonance in a superconducting system which is essential for the construction of various lossless electromagnetic wave sources such as terahertz devices.

REFERENCES

- [1] www.goldennumber.net.
- [2] R Coldea, D A Tennant, E M Wheeler, E Wawrzynska, D Prabhakaran, M Telling, K Habicht, P Smeibidl, K Kiefer, "Quantum criticality in an Ising chain: experimental evidence for emergent E8 symmetry", *Science*, 327, 177, 2010.
- [3] X F Pang, Y PFeng, *Quantum Mechanics in Nonlinear Systems* World Scientific Publishing, Singapore, 2005.
- [4] Physics Survey Committee, *Physics Through the 1990's Condensed Matter Physics*, National Academy Press, Washington DC, 1986.
- [5] Ü. Onbaşlı, Z. Güven Özdemir, and Ö. Aslan, "Symmetry breakings and topological solitons in mercury based d-wave Superconductors", *Chaos Solitons Fractals*, vol. 42, pp. 1980-1989, 2009.
- [6] Ö Aslan, Z. Güven Özdemir, S S Keskin, Ü Onbaşlı, "The chaotic points and XRD analysis of Hg-based superconductors", *Journal of Physics: Conference Series*, 153, 012002, 2009.
- [7] Ö. Aslan Çataltepe, "Some chaotic points in cuprate superconductors", in: *Superconductor*, A.M. Luiz, Ed., India: Sciy Company, 2010, pp. 273-290. (Available from: <http://www.intechopen.com/articles/show/title/some-chaotic-points-in-cuprate-superconductors>)
- [8] Z. Güven Özdemir, Ö. Aslan, and Ü. Onbaşlı, "Terahertz oscillations in mercury cuprate Superconductors", *Pramana-J. Phys.*, vol. 73, pp. 755-763, 2009.
- [9] Ö Aslan, Z. Güven Özdemir, Ü Onbaşlı, Correlation Between The Anisotropy and The Effective Mass of The Quasi-Particles in Oxide Superconductors, *AIP Conference Proceedings* 899 (1), 271-272, 2007.
- [10] Ü Onbaşlı, Z. Güven Özdemir, "Superconductors and Quantum-Gravity" in *Superconductor* edited by A M Luiz, Sciy Company, India, 2010, p.291 (Available from: <http://www.intechopen.com/books/superconductor/superconductors-and-quantum-gravity>)
- [11] Ö. Aslan Çataltepe, "Mercury cuprates bring symmetry breaking of the Universe to laboratory", in: *Lifetime of the Waves From Nano To Solitons In My Life*, Ü. Onbaşlı, Ed., Kerela, India: Transworld Research Network, 2012, pp. 215-243. (Available from: http://www.tnres.com/ebook/uploads/onbaslicontent/T_1350723744_5%20Onbasli.pdf)
- [12] K Kadowaki, I Kakeya, K Kindo, "Observation of the Nambu-Goldstone Mode in the High Temperature Superconductor $\text{Bi}_2\text{Sr}_2\text{CaCu}_2\text{O}_{8+\delta}$.", *Europhys.Lett.*, 42, 203, 1998.
- [13] P.W. Anderson, "Plasmons, Gauge Invariance, and Mass", *Phys. Rev.*, 130, 439, 1963.
- [14] Z. Güven Özdemir, A Aslan Çataltepe, Ü Onbaşlı, "The Correlation between the Double Helix Quantum Wave in d-Wave Superconductors and Human DNA", *Acta Physica Polonica A*, 121, 13, 2012.
- [15] Z. Güven Özdemir, Ö. Aslan, and Ü. Onbaşlı, "Determination of c-axis electrodynamic parameters of mercury cuprates", *J. Phys. Chem. Solids*, vo. 67, pp. 453-456, 2006.
- [16] Z. Güven Özdemir, Ö. Aslan, and Ü. Onbaşlı, "Calculation of microwave plasma oscillations in high temperature Superconductors", in: *The 7th International Conference on Vibration Problems (ICOVP 2005)* Springer Proceedings in Physics

- 111, E. İnan, E. Kırış (Eds.), Dordrecht, The Netherlands: Springer, 2007, pp. 377-382.
- [17] R Ferrell, R Prange, "Self-Field Limiting of Josephson Tunneling of Superconducting Electron Pairs", Phys. Rev. Lett., 10, 479, 1963.
- [18] V V Schmidt, in The Physics of Superconductors, Introduction to Fundamentals and Applications edited by P Müller and A V Ustinov Springer, Erlangen, p.81,1997
- [19] M Tinkham, Introduction to Superconductivity, McGraw-Hill, New York, 1996.
- [20] P W Anderson, The Theory of Superconductivity in the High-Tc Cuprate Superconductors, Princeton University Press, New Jersey, 1997.
- [21] M S Li, "Paramagnetic Meissner effect and related dynamical phenomena", Phys. Rep., 376, 133, 2003.
- [22] Z. Güven Özdemir, Ö. Aslan, and Ü. Onbaşlı, "Terahertz oscillations in mercury cuprate Superconductors", Pramana-J. Phys., vol. 73, pp. 755-763, 2009.

Failure Analysis of Jet Turbine Engine High Pressure Nozzle Material Made of Cobalt Based Super Alloy

Ozan Çoban, Özgür C. Arslan, and Tuba Karahan

Metallurgical and Materials Engineering Department, Istanbul Gedik University
Kartal Campus, Kartal/Istanbul, 34876, Turkey
ozan.coban@gedik.edu.tr; ozgurcagatayarslan@outlook.com; tuba.karahan@gedik.edu.tr

Received: 27.11.2018 Accepted: 24.12.2018

Abstract: In this study, we carried out the failure analysis based on metallographic research of a cobalt superalloy material which had been used in jet turbine engine. The failure analysis was made by chemical composition analysis, hardness test and microstructural researches after metallographic sample preparation on the material which had operated about 30000 hours and damaged. Macro cracks which can be seen by visual inspection have been detected on the cobalt based superalloy nozzle material's some surfaces which had exposed to high temperature and high pressure fuel-air mixture. After the metallographic sample preparation and optical and electron microscope investigation, it has been determined that the main reason of the failure is coarse and continuous morphology M_7C_3 carbide precipitations on the grain boundaries and as a result of that, stress corrosion cracking has moved through that grain boundaries which have been embrittled and weakened against high temperature corrosion. Also, after consideration of the chemical composition on the damaged area of material, it has been detected that, owing to the usage of carbon content fuel during operation, carbon diffusion at high temperature into the material had occurred. So, with high carbon content in the material, the type and morphology of the carbides had changed and caused the failure.

Keywords: Failure analysis, jet engine and turbine, nozzle, cobalt base superalloy, carbide transformation, stress corrosion, microstructure, optical microscopy.

1. INTRODUCTION

Nickel and cobalt based superalloys are the materials which have been widely used in both aerospace industry and also gas turbines. Their excellent creep resistance, high temperature corrosion resistance and also having higher strength at elevated temperatures make cobalt based super alloys more profitable in comparison with nickel based superalloys [1]. In this sense, cobalt based superalloys are widely used in some critical parts of jet engines. One of these critical materials is high temperature nozzle. The task of this material which is used as first stage high pressure nozzle in jet engines and power turbines is conveying the hot gas flow that released from the combustion chamber most efficiently and with best angle through the rotating parts of turbine. Therefore, more than mechanical stresses, this nozzle is exposed to thermal loadings and also bending stresses due to the gasses which have high temperature and pressure. In this case, the possible material failure mechanisms which can be occurred during these operation conditions are creep, creep-fatigue, thermal fatigue, oxidation and high temperature corrosion [2].

The most important factor that determines the performance of the nozzles made of cobalt based

superalloys is their microstructures. The microstructures of these materials might be changed during the operation because of high temperatures. The phases in the microstructure, morphologies of them and the regional chemical compositions can be changed. Therefore, the failure analysis is carried out in the foreseen lifetime of the material and repair or renewal decision is made according to the analysis. The basic method for failure analysis of these type of cobalt based superalloys is metallography. The sample prepared by metallographic sample preparation processes is subjected to the optical microscopy and/or electron microscopy investigation. As a result of microscopic investigation acting like a detective searching a crime, according to the failure or crack structure and according to the phase changes in the microstructure of material, the failure mechanism is determined.

The aim of that study is to determine the reason of the failure on the first stage high pressure nozzle material which had operated approximately 30,000 hours while it had been predicted to operate for 70,000 hours. In addition to that, another aim of that study is to determine the correct metallographic sample preparation processes of cobalt based superalloys. By carrying out optical microscopy and electron microscopy investigations, determination of the

failure mechanism on the nozzle and according to the results, improving the service life of the material are the main targets of that study.

2. MATERIALS AND METHODS

The material on which failure analysis has been carried out is a cobalt based superalloy which had operated for 30,000 hours inside the General Electric CF6-50 high bypass turbofan engine as first stage high pressure conveying nozzle and it has been shown on Figure 1.

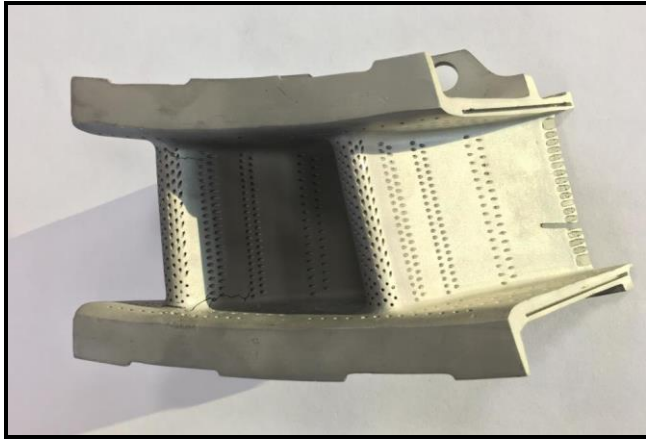


Figure 1. First stage high pressure nozzle

2.1. Sampling

After visual inspection, sampling was carried out from the macro crack zones and also non-damaged parts for comparison. The sampling zones of the sample and the names of zones were shown on Figure 2.



Figure 2. Sampling zones

The cutting process for sampling step of metallography was carried out by using Metacut 251 abrasive cutting machine which has SiC cutter disk and liquid cooling system in Istanbul Gedik University Metallurgical and Materials Engineering Laboratory.

2.2. Hot Molding

Hot molding method was preferred in order to both make cut parts hand-held and inserted into neatness for all next steps which are grinding-polishing, etching and microscopy. Ecopress 50 Hot Molding Machine and bakalite and acrylic powders were used for molding process. The temperature was 190⁰C, the pressure was 130 bar and the duration was 3 minutes for sintering and 3 minutes for cooling.

2.3. Grinding – Polishing

After molding, grinding and polishing processes were applied to the samples by Metkon Forcipol 2V machine which is located in Istanbul Gedik University Metallurgical and Materials Engineering Laboratory. SiC grinding disks were used as abrasives during grinding process. The rotational speed was 300 rpm during both grinding and polishing. For polishing, 0.25 µm mono crystalline diamond suspension and diamond based lubricant were used.

2.4. Etching

For microstructural analysis with optical microscope; from optic physics and inorganics chemistry aspects, the requirement is creating metallurgical contrast on the surface to be investigated. In order to actualize it, a chemical called etchant is used.

In order to carry out optical microscopy investigation, etching process was applied to the polished samples with convenient etchants and in optimum etching durations. We applied the both chemical etching and electrolytic etching methods.

For chemical etching, Kallings No:2 etchant was prepared with 5 gr CuCl₂, 100 ml hydrochloric acid (HCl) and 100 ml ethyl alcohol (ethanol). For electrolytic etching, a solution which includes 10 ml HCl, 10 gr CrO₃ and 100 ml distilled water was prepared. The sample was attached to the positive pole of a direct current power supply as anode and 304 stainless steel as cathode to the negative pole. Both anode and cathode were submerged into the etchant solution and 6 V voltage has been applied for 10 seconds duration. Immediately after etching, the sample was washed thoroughly with ethyl alcohol and water and dried with warm air flow.

2.5. Microstructural Investigation

After the sample was etched in correct duration and correct etchant, the metallurgical phases were dissolved in different amounts from the aspect of electrochemistry, in micro scale. And the phases reflected the light characteristically due to their spectrum difference of each. We could see the microstructure of the cobalt based superalloy, which had been damaged in micro and also macro scale, by using BAB Software Optical Microscope.

For physical structural investigation and chemical composition investigation of critical parts of micro crack, we used EDS equipped High Vacuum 20 kV scanning electron microscope which is located in Yalova University Laboratory.

2.6. Chemical Analysis and Hardness Test

For failure analysis of nozzle sample, beside the metallographic characterization, also chemical analysis and hardness tests were carried out by XRF Spectrometer, Carbon-Sulphur Analyser and Digirock HV30 Vickers Hardness Testing Machine in Gedik Holding Research and Development Laboratory and Gedik Test Center.

3. RESULTS AND DISCUSSIONS

As the first step for failure analysis of the sample which had operated for 30,000 hours in turbine engine combustion chamber, visual inspection was carried out and macro fractures and macro cracks were detected on outer surface as shown on Figure 3.



Figure 3. Failure zone detected by visual inspection

As the result of visual inspection, 2 main fracture failures and 1 macro crack failure were detected. The failure has occurred on a zone on which hot and high pressure gas might have been circulated and which is close to the connection zone with the platform. Both high temperature and pressured gas were existed around that zone and also stresses might have occurred on it. For that reason, it has been thought that the failure mechanism would be a stress-corrosion cracking.

After visual inspection, we decided to carry out optical microscopy investigations on the surface around the macro crack. Macro crack could give us some predictions about the reason of failure because it can represent the main fracture failures.

Before metallographic sample preparation and microstructure analysis processes, chemical composition analysis was carried out on the sample which had been taken far from the failure zone. According to the XRF elemental analysis result given on Table 1, it could be seen

that the material is cobalt based superalloy and the chemical content values are approximate with the values of FSX 414.

Table 1. Chemical analysis result

| Element | % by weight | Element | % by weight |
|---------|-------------|---------|-------------|
| Ni | 23.8425 | Ti | 0.4329 |
| C | 0.2080 | Co | 42.0733 |
| W | 6.3959 | Cr | 22.6896 |
| Mo | 0.3453 | Si | 0.9519 |
| Fe | 0.4794 | Ta | 0.8566 |
| Al | 1.4629 | Others | 0.2617 |

Before the microstructural analysis, hardness tests were carried out on different points which have particular distance to macro crack center line. Hardness test results have been shown on Figure 4. Hardness values are approximate to each other in macro scale. Therefore, it was thought that locational hardening due to heat treatment effect or softening due to grain size growth should not have been occurred on the microstructure.

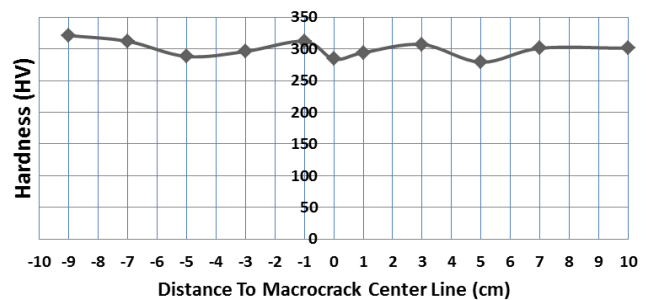


Figure 4. Hardness test result

After hardness tests, metallographic sample preparation and optical microscope investigation were carried out and as results, the microstructures below were obtained. According to these microstructures;

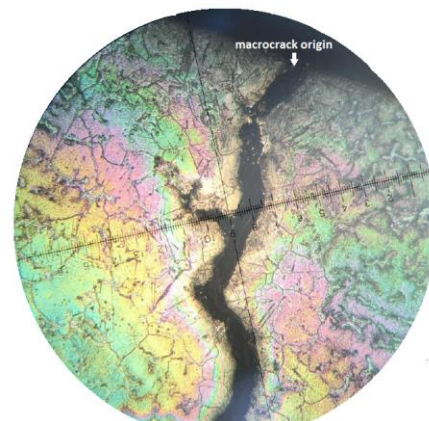


Figure 5. Microstructure of macro crack zone (100x – electrolytic etched with 6% chromic acid + 10% HCl)

On Figure 6, the microstructure of the area that macro crack had occurred and propagated through has been given. When we looked at the structure of the crack, we thought that macro crack could have occurred by growth of intergranular micro cracks. In order to understand the mechanism of failure, first, microstructural investigation of non-damaged zone was carried out. On Figure 6, the microstructure taken from zone 3 has been given.

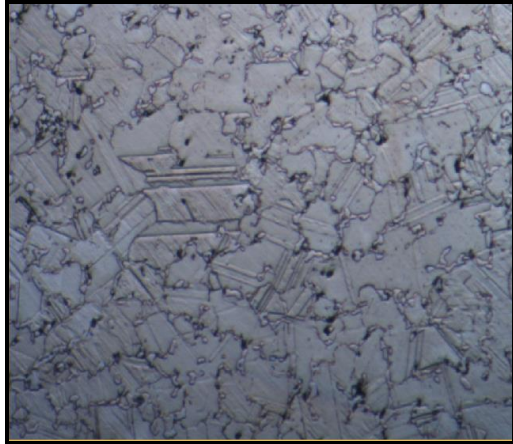


Figure 6. Microstructure of cobalt based superalloy (100x – electrolytic etched with 6% chromic acid + 10% HCl)

Twinnings inside the austenitic matrix of face centered cubic (FCC) structure and also carbide precipitations on grain boundaries and inside the grain can be seen on the microstructure that given on Figure 6. The transformation of lattice structure from face centered cubic (FCC) to hexagonal closed pack (HSP) structure occurs on cobalt based superalloys over 417⁰C. In order to avoid this transition, cobalt based superalloys are alloyed with nickel [3]. Because our material includes nickel over than 10 %, it could be understood that the lattice structure of the matrix is FCC. The basic phases that affect the mechanical properties of cobalt based superalloys are the carbide phases. Therefore, the microstructures of carbides have been investigated and the results were obtained as;

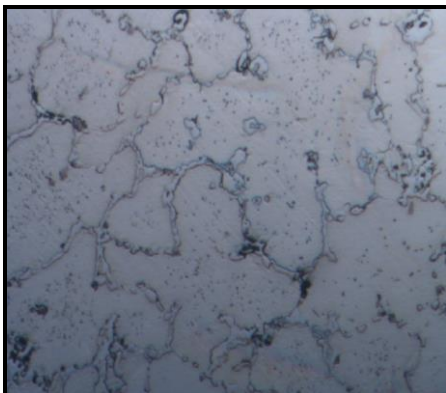


Figure 7. Microstructure of carbides obtained from non-damaged zone (100x - electrolytic etched with 6% chromic acid + 10% HCl)

The microstructure obtained from zone 2 but far from the main fractures and macro crack has been given on Figure 7. It can be seen on microstructure that spherical and chain type carbides have precipitated on the grain boundaries. However it has been detected that, the morphologies of carbides are changing by approaching to the macro crack. When the microstructure, obtained from closer point to macrocrack, given on Figure 8 is considered, it can be seen that some of the spherical and chain type carbides, are replaced by continuous formed carbides.

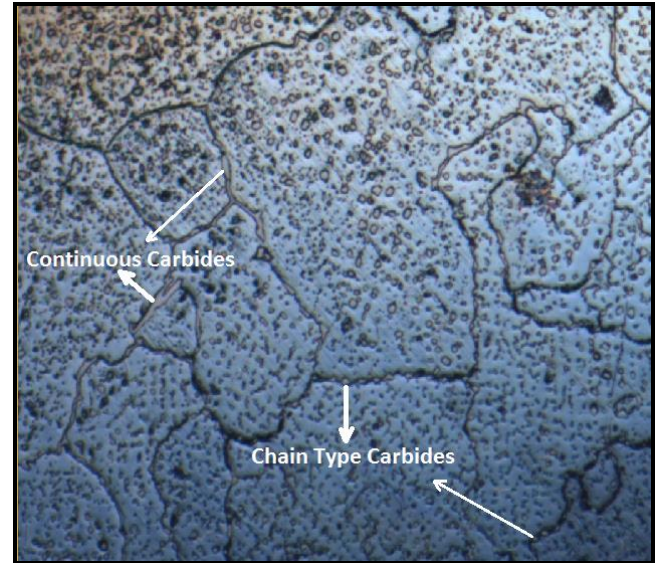


Figure 8. Microstructure of carbides obtained from closer zone to macrocrack (100x - electrolytic etched with 6% chromic acid + 10% HCl)

When we get closer to the macro crack, it can be seen that the amount of continuous formed carbides are increasing as shown on the microstructure that given on Figure 9.

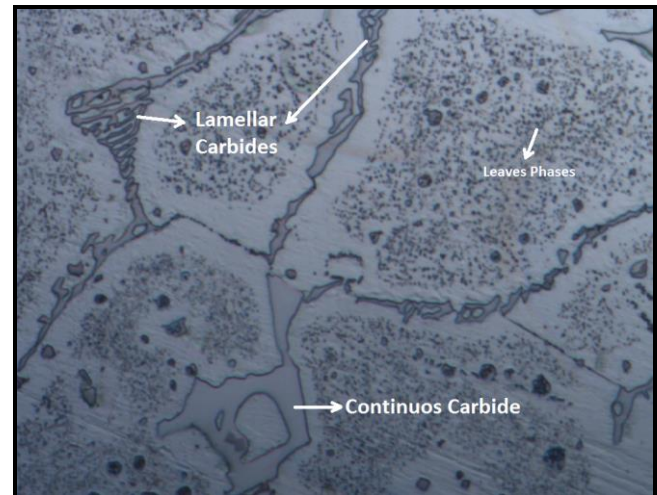


Figure 9. Microstructure of carbides near the macrocrack (200x - electrolytic etched with 6% chromic acid + 10% HCl)

Lamellar morphology carbides and continuous formed carbides precipitated on grain boundaries and also other types of carbides and leaves phases inside the grains can be seen on the microstructure given on Figure 9.

After the detection of carbide morphology changes through the macrocrack, we decided to investigate the origin, sides and tip of the macrocrack and the microstructures are;

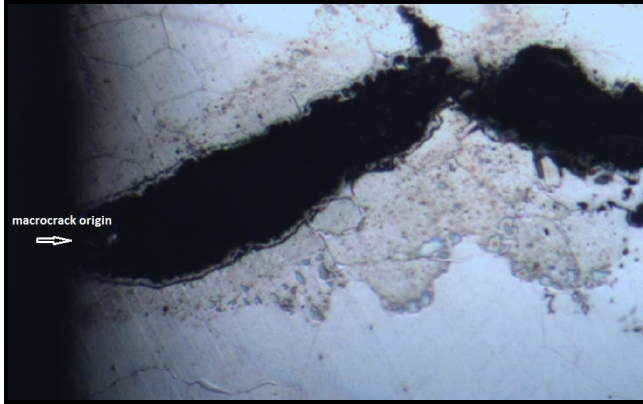


Figure 10. Microstructure of macrocrack origin (100x – slightly chemically etched with Kallings No:2)

Microstructure of macrocrack origin zone, which had been slightly chemically etched, has been given on Figure 10. Due to the fact that oxides are electrochemically affected by etchants more than metallic phases, it has been thought that the brown colored parts surrounding the crack could be hot corrosion products. After that estimation, we decided to carry out electrolytic etching.

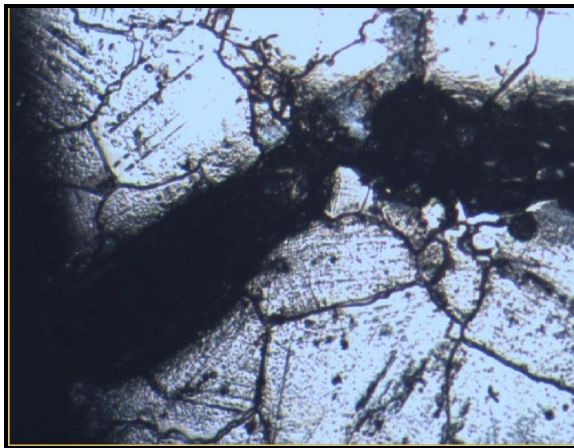


Figure 11. Microstructure of macrocrack origin (100x – electrolytic etched with 6% chromic acid + 10% HCl)

On the microstructure of macrocrack zone has been given on Figure 11, intergranular corrosion cracks and continuous carbides on grain boundaries could be seen. After that we decided to investigate the tip zone of the crack in order to see propagation mechanism of it.

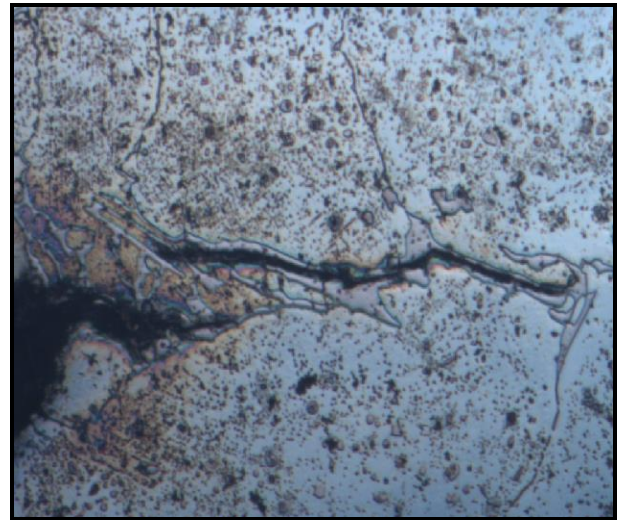


Figure 12. Microstructure of the tip zone of crack (200x slightly chemically etched with Kallings No:2)

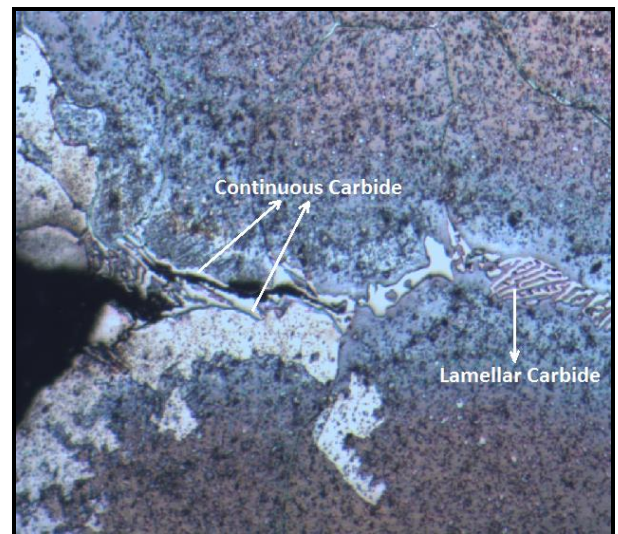


Figure 13. Microstructure of the tip zone of crack (100x - electrolytic etched with 6% chromic acid + 10% HCl)

As it can be seen on Figure 12 and Figure 13 which shows the microstructure of tip zone, macrocrack has propagated up to a point and then it continued as micro crack on its path passing through the continuous formed carbides that have precipitated on the grain boundaries as it can also be seen on Figure 14 which shows the microstructure of micro crack tip. It can also be seen that microcrack propagation stops and possibly nanocracks propagation occurs up to lamellar morphology carbides which have also precipitated on grain boundaries.



Figure 14. Microstructure of microcrack tip (200x - electrolytic etched with 6% chromic acid + 10% HCl)

After optical microscopy analysis we considered the results and decided to carry out electron microscope analysis in order to determine the types of carbides chemically and morphologically. On the Figure 15 and Figure 16, SEM images of crack zone have been shown. It can be seen that macrocrack had propagated mostly through grain boundaries zone. And also corrosion products can be seen around the macrocrack.

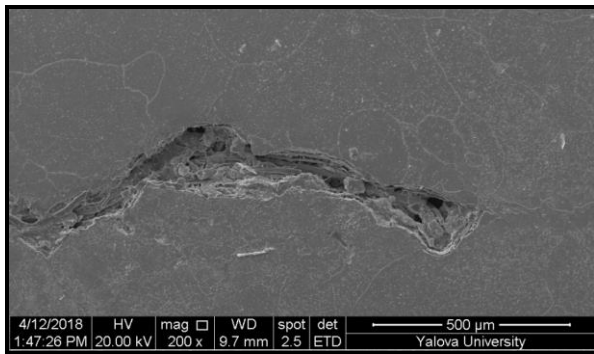


Figure 15. SEM image of macrocrack

As shown on the SEM image of macrocrack tip zone on Figure 16, macro crack propagation is blocked by semi lamellar semi continuous morphology carbide precipitates. However, macrocrack had found a path for propagation as microcrack. As it can be seen on Figure 17, the path of microcrack is surrounded by continuous morphology carbides. It means that microcrack had propagated through the continuous carbides on grain boundaries.

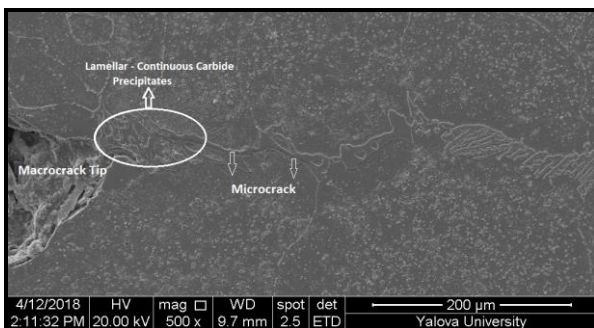


Figure 16. SEM image of macrocrack tip zone

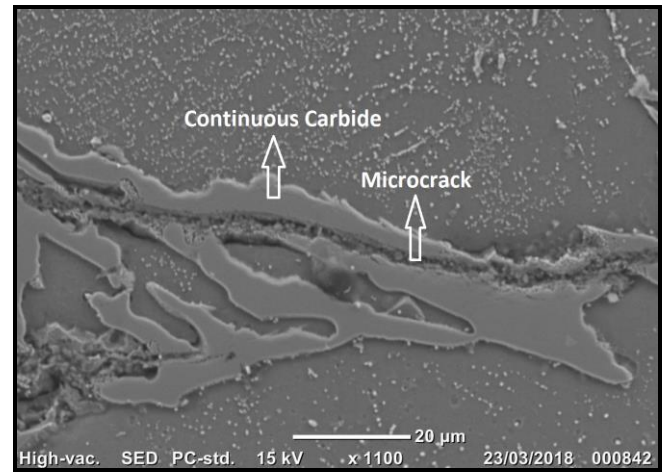


Figure 17. SEM image of microcrack

In cobalt based superalloys, $M_{23}C_6$ and M_7C_3 carbides form during the last stage of solidification and the carbide type is basically related to Cr/C ratio. While M_7C_3 carbides occur at lower Cr/C ratio, $M_{23}C_6$ carbides occur at higher Cr/C ratio [4].

SEM-EDS analysis was carried out on the points shown by blue rectangles on Figure 18. According to the results given on Table 2, continuous carbides include higher carbon and lower wolfram and molybdenum in comparison with lamellar carbides. When we compare the Cr/C ratios, while the ratio of continuous carbide is 2.012, the ratio of lamellar carbide is 2.904. As the result of SEM-EDS analysis, it could be understood that lamellar carbides are $M_{23}C_6$ and continuous carbides are M_7C_3 .

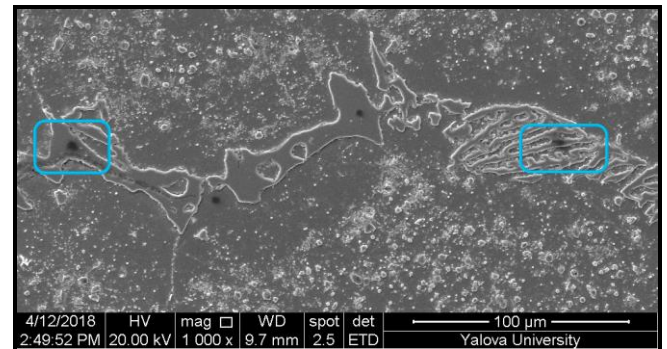


Figure 18. SEM-EDS image of carbides

Table 2. SEM-EDS analysis results

| | C% | Mo% | Cr% | Co % | Ni % | Ta % | W% |
|----------------------------|-------|------|-------|------|------|------|------|
| Lamellar Carbide | 18,31 | 6,97 | 53,18 | 8,97 | 1,48 | 1,57 | 9,52 |
| Continuou s Carbide | 27,32 | 1,72 | 55,15 | 7,52 | 1,06 | 1,6 | 5,63 |

In super alloys, dense and continuous carbides expedite crack occurrence and propagation, decrease ductility and toughness by 30 % and shorten the lifetime of the material [5]. This could be seen on this study, too. As it can be seen on the microstructures obtained by both optical microscopy

and electron microscopy investigations, the failure that had occurred on the nozzle, the macrocrack and microcrack, had propagated through M_7C_3 type continuous carbides and the propagation had been blocked or slowed down by $M_{23}C_6$ type lamellar carbides.

Table 3. Carbide types in cobalt based superalloys [6]

| Carbide Type | Elements | Morphology |
|--------------|--------------------|---|
| MC | Ti, Nb, Zr, Hf, Ta | Spherical, cubic or disordered shaped as particles and shiny |
| M_7C_3 | Cr | As blocks, continuous formed and extends through grain boundaries |
| $M_{23}C_6$ | Cr, W | Spherical, layered or lamellar morphology and on grain boundaries |
| M_6C | Mo, W | Randomly dispersed, pinkish white |

The carbide types that occur in cobalt based superalloys are given on Table 3. The mole ratio of carbon, corresponding to 1 mole of metal, decreases when descend through the below of the table. In other words, in the presence of these elements, the amount or the possibility of formation of upper side carbides increases with the increase of carbon content.



As it can be indicated with (1), when the carbon content increases, carbide formation can occur and beside the lamellar $M_{23}C_6$ type carbides ($Cr_{23}C_6$ and $W_{23}C_6$), continuous M_7C_3 type carbides (Cr_7C_3) precipitate on grain boundaries. After that consideration, in order to see if there were any carbon content difference between the non-damaged parts and damaged part of the nozzle, we decided to carry out carbon - sulphur analysis to the sample, which has been taken from the part of the nozzle on which macrocrack had occurred. According to the C-S analysis results, strikingly, while non-damaged part of the nozzle includes 0.2 % carbon, the part of the nozzle on which failure occurred includes 0.4 % carbon. As the result of carbon analysis, it can be claimed that because of carbon diffusion into the part of the nozzle from hot gas including unburnt carbon, the carbon content of microstructure had increased and carbide transformation ($M_{23}C_6 \rightarrow M_7C_3$) had occurred.

In all super alloys, carbides are the weak phases against oxidation. In order to minimize the high temperature corrosion failure, carbides need to be small and discontinuous [7]. When all the microstructures are considered in our study, it can clearly be seen that the crack had propagated through continuous morphology carbides. In order to avoid this occurrence, the carbide transformation needs to be blocked. As a resolution advisory, molybdenum and/or wolfram contents could be increased in order to succeed it. These elements increase the potential of

occurrence of M_6C carbides and M_6C carbide occurrence can decrease the potential of M_7C_3 carbide occurrence. In addition, as it can be indicated with (2), these elements increase the possibility of carbide transformation from M_7C_3 to $M_{23}C_6$. Thus, these alloying elements could help to obtain more ductile carbides on the grain boundaries and could prevent grain boundary embrittlement. So, increasing Mo and W alloying elements could increase the lifetime of a cobalt based superalloy nozzle which operates under these kinds of conditions like exposing carbon diffusion from the hot gas which includes unburnt carbon.



According to the carbide transformations during the service according to the (1) and (2), beside the wolfram and molybdenum content increase advisory for solution, also the content of MC type carbide making elements could be increased in order to minimize the $M_{23}C_6 \rightarrow M_7C_3$ transformation due to high chromium activity. Owing to both carbonization due to diffusion and also carbon occurrence due to transformations, instead of carbon's making brittle continuous Cr_7C_3 carbides on grain boundaries, MC type carbides such as TiC, NbC, TaC could be provided to be occurred inside the grain.

The elements, advised to be increased in cobalt based super alloy which is to be used as first stage high pressure nozzle in a jet turbine engine, in a sense, would replace with chromium and owing to this we could provide both high stress corrosion resistance and also could increase the high temperature corrosion resistance. Because in the presence of these elements, instead of brittle Cr_7C_3 carbides, more ductile $Cr_{21}(W,Mo)_2C_6$ carbides would occur on grain boundaries and also it can be provided that chromium would make Cr_2O_3 layers, which increases the corrosion resistance, instead of making carbides.

4. CONCLUSION

The cobalt based super alloy sample; which had been used as nozzle for conveying the hot and high pressure air-fuel mixture, released from combustion chamber, through first stage high pressure turbine; could have operated 30,000 hours while it had been estimated to operate 50,000-70,000 hours because of failure. In our failure analysis study, we detected the reason of the failure as carbide transformation due to carbon diffusion on to the material from circulated gas which might have included unburnt carbon. Related to the carbon diffusion, because of $M_{23}C_6 \rightarrow M_7C_3$ carbide transformation, the grain boundaries had embrittled and weakened against stress corrosion crack propagation due to the fact that continuous formed brittle M_7C_3 carbides are acting like a pathway for crack propagation while lamellar formed ductile $M_{23}C_6$ carbides are acting like a block.

We also estimated that the lifetime of the nozzle could be increased by preventing carbide transformation by increasing the molybdenum and wolfram content of the material, because they increase the possibility of $M_{23}C_6$

carbide occurrence at elevated temperatures despite carbon diffusion during service. In addition to molybdenum and wolfram content increasing advisory, we also estimated that increasing MC carbide making alloying elements content such as Ti, Nb, Ta and Hf could be beneficial for cobalt based superalloys which operate at high temperatures and under the conditions of carbon diffusion might be occurred.

Space and aerospace industry are continually developing engineering application industries. At that point, material failures should be minimized for these kinds of critical parts such jet engine parts. In order to minimize the failures, failure analysis studies should be increased and developed.

ACKNOWLEDGMENT

First and foremost, we give special sincerest gratitude to Prof. Dr. Muzeyyen Marsoglu for her psychological and scientific supports and Prof. Dr. Ahmet Topuz and Prof. Dr. Sunullah Ozbek for their support on the study. In addition, we would like to thank Gedik Holding Research and Development Department and Gedik Test Center for chemical analysis and mechanical tests and also Yalova University for electron microscopy analysis.

REFERENCES

- [1] Gui, W., Zhang, H., Yang, M., Jin, T., Sun, X., Zheng, Q. "Influence of type and morphology of carbides on stress-rupture behavior of a cast cobalt-base superalloy", *Journal of Alloys and Compounds* 728 pp 145-151, (2017)
- [2] Pallos, K. J., "Gas Turbine Repair Technology," Paper No. GER 3957B. (2001)
- [3] ASM Specialty Handbook Heat Resistant Materials, Metallurgy, Processing and Properties of Superalloys, p.237.
- [4] Gui W. , Zhang, H. , Yang, M. , Jin, T. , Sun, X. , Zheng, Q., The investigation of carbides evolution in a cobalt-base superalloy at elevated temperature, *Journal of Alloys and Compounds* 695, pp. 1271 – 1278. (2017)
- [5] Koul AK, Castillo R., "Assessment of service induced microstructural damage and its rejuvenation in turbine blades." *Metall Trans* 1998;19(A):2049–56.
- [6] ASM Specialty Handbook Heat Resistant Materials, Metallurgy, Processing and Properties of Superalloys, p. 227.
- [7] Pettit, F.S., Maier, G., "Oxidation and Hot Corrosion of Superalloys", *Metallurgical and Materials Engineering Department, University of Pittsburgh*, p.661.

Influence of Local Soil Conditions on the Structural Design and Associated Costs

Harun İnce¹, Ebru Toy², and Mert Tolon³

¹ Civil Engineering Graduate Program, Institute of Science and Technology, İstanbul Gedik University
Kartal, İstanbul, Turkey
harun52.hn@gmail.com

^{2,3} Civil Engineering Department, Faculty of Engineering, İstanbul Gedik University
Kartal, İstanbul, Turkey
ebru.toy@gedik.edu.tr; mert.tolon@gedik.edu.tr

Received: 16.11.2018 Accepted: 21.12.2018

Abstract: It is known that earthquakes occur along the faults as a result of the tectonic plate movements [1]. The North Anatolian, Northeast Anatolian and East Anatolian Faults create three major fault lines in Turkey. In connection with these fault lines, there are various studies concentrated mostly on the seismicity and the topic of earthquake hazard has been examined by many researchers until today. According to the literature, to cope with earthquake related problems, an utmost attention should be given to the existing building stock and currently available design principles used for earthquake resistant structures in the country. In general, the damage to buildings stem from the lack of knowledge and experience in the field, lack of soil survey database, and structural irregularities in plan and elevation. According to building design codes, the seismic load acting on the structures depends on the seismic zone, the soil type, its period of vibration and the mass of the building [2]. In the present study, the main objective is to evaluate the influence of local site effects on the seismic response of buildings in terms of 2018 Turkish Seismic Design Code provisions and to analyze their impact on the cost of construction of buildings. In the study, a two-story reinforced concrete-framed building (residential house) is used as an example. Using the architectural layout of the building, the thickness of floor slabs and column size are determined. The construction cost is estimated roughly by considering unit costs method. The cost of the reinforced concrete structure is determined by considering 2017 unit price list, specified by the Ministry of Environment and Urbanization [3]. It's quite clear that the cost of structure built on soil class ZD is more expensive than the cost of the one built on the soil class ZA. The cost difference is around 22,57% between soil classes ZA and ZD.

Keywords: Earthquake, Turkish Seismic Design Code 2018, Method of Finite Elements, Soil Class, Construction Work Items and Current Unit Prices

1. INTRODUCTION

The Earth's crust, or the lithosphere, is a living entity that constantly changes its internal and external structure. Tectonic plates, gigantic segments of Earth's crust are always moving. We cannot feel this shifting and change in our daily lives. Continuous and slow movements, defined as continent forming movements, are about 1 to 10 mm in size per year. However, there are rapid crust movements that are felt by people and last only seconds, which are called as earthquake. Earthquakes occur mostly due to large elastic fractures along the fault line [1].

Structural safety in a building can be achieved by doing basic structural calculations to provide safety against these large earthquakes. Engineering can be expressed as the art of finding the optimum solution between durability, aesthetics and economy in production. A structure must

provide strength, durability, economy, function and aesthetics together. The most important task for engineers on the subject is to combine those elements [4].

In general, the common reasons for damage to buildings are; lack of knowledge and experience in the field, lack of soil survey database, and structural irregularities in plan and elevation. The earthquake forces that acting on structures varies depending on the soil class, the regional seismic ground accelerations and the type of structure [2].

Since the total earthquake load that will affect the structure depends, to a great extent, on the earthquake zone and the local soil class, the seismic response of structures located in that region will also be different [5]. One of the main reasons for buildings sustaining significant damage during an earthquake is that the change in soil class from Z1 to Z4 leads to increase the predominant period of earthquakes. Consequently, the period of vibration of the

building will be closer the predominant period of earthquake for soil classes Z3 and Z4 [11].

According to the earthquake zones and local soil class, the expected earthquake intensity will be different from each other. Therefore, the structural dimensions and / or reinforcement details of the structural system and thus the cost of the building will change [6].

2. APPROACH

2.1 Selection of Earthquake Ground Motion for Performing Analyses

In 1996, Seismic Zoning Map of Turkey on the basis of probability methods published by the Ministry of Public Works and Settlement. Table 1 shows the distribution of seismic hazard risk in Turkey. According to this study, 66% of Turkey's surface area is within the 1st and 2nd degree earthquake zones, in other words active fault zones (zone of fractures along the fault line) 71% of population resides in that region [7].

Table 1 Distribution of seismic hazard risk in Turkey, 1996 [8].

| SEISMIC HAZARD ZONE | SURFACE AREA (%) | POPULATION (%) | INDUSTRY (%) | DAMS (%) |
|----------------------------|------------------|----------------|--------------|------------|
| 1st Degree Earthquake Zone | 42 | 45 | 51 | 46 |
| 2nd Degree Earthquake Zone | 24 | 26 | 25 | 23 |
| 3rd Degree Earthquake Zone | 18 | 14 | 11 | 14 |
| 4th Degree Earthquake Zone | 16 | 15 | 13 | 17 |
| TOTAL | 100 | 100 | 100 | 100 |

As a result of research and analysis done, 1st degree earthquake zone which has high risk level of seismic activity in Turkey is selected as an input (Figure 1).

2.2 TSDC 2018– Local Site Classes

By observing Figure 1 and Figure 2, it is apparent which seismic zones need to be analyzed and designed in detail to avoid the negative consequences of future seismic events. In addition to tectonic activity, there exist important additional factors, such as soil condition. These factors that directly affect the seismic response of structures, should be accounted for in the seismic analysis and design procedure of any building type. In Turkish Seismic Code, there are four different soil groups (ZA, ZB, ZC and ZD) which are classified according to the geological subsurface conditions. These groups further divided into local site classes (Z1, Z2, Z3 and Z4) dependent on the topmost soil layer thickness (h).

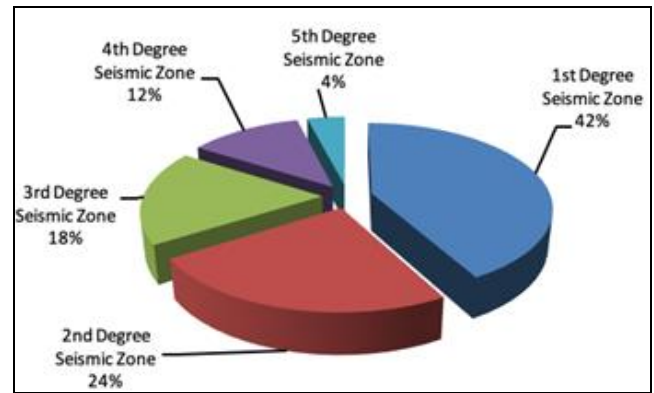


Figure 1. Pie chart presenting the percentages of the seismic hazard Risk in Turkey.

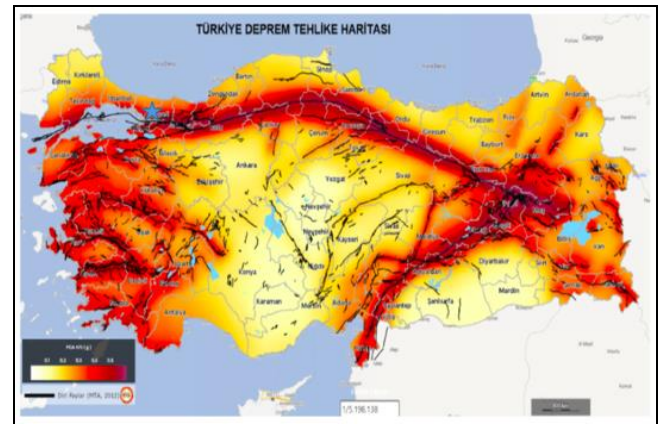


Figure 2. Turkey's seismic hazard map [10].

In order to predict the seismic behavior of structures under strong ground motion levels, the local soil condition at a site must be taken into account due to its amplifying or de-amplifying effects in the response spectrum [12].

For instance, in order to advance the understanding of amplification effects of the soil, the Building Research Institute (BRI) of the Ministry of Construction and the Association for Promotion of Building Research (APBR) in Sendai city, Japan in 1983 started to accumulate earthquake records after installation of seismic recording sites. In the study, the examined surface geology has a variety of soil conditions including outcrop rock site, reclaimed land, and soft soil ground. As a result of this study, although the project duration was not enough to collect enough data, the broad range of findings on the soil amplification and variation of subsurface earthquake motions were obtained by researchers [13].

According to the Turkish Seismic Design Code (TSDC 2018), the soil groups classified as ZA, ZB, ZC and ZD depending on the design acceleration spectrum. If the soil profile belongs to the ZA soil group, the ground display solid, hard rock form; ZB local soil classes display less weathered, medium-solid rocks texture; ZC local floor grade very tight sand, gravel and hard clay layers; ZD local ground grade gravel or clay layers; ZE local soil grade loose sand, soft clay floors; the ZF soil layers require site-specific

research and evaluation. The spectral acceleration coefficients of these soil groups are shown in Table 2. When Turkish Earthquake Code 2007 (TEC) and TSDC 2018 regulations are examined, it's accepted that the Z1 soil class reflects the characteristic of the ZA local soil group.

Table 2. Spectral acceleration coefficients [9].

| Soil Group | $S_1 \leq 0.1$ | $S_1 = 0.2$ | $S_1 = 0.3$ | $S_1 = 0.4$ | $S_1 = 0.5$ | $S_1 \geq 0.6$ |
|------------|----------------|-------------|-------------|-------------|-------------|----------------|
| ZA | 0.8 | 0.8 | 0.8 | 0.8 | 0.8 | 0.8 |
| ZB | 0.8 | 0.8 | 0.8 | 0.8 | 0.8 | 0.8 |
| ZC | 1.5 | 1.5 | 1.5 | 1.5 | 1.5 | 1.4 |
| ZD | 2.4 | 2.2 | 2.0 | 1.9 | 1.8 | 1.7 |
| ZE | 4.2 | 3.3 | 2.8 | 2.4 | 2.2 | 2.0 |

3. STRUCTURAL MODELING AND ANALYSIS

3.1 Details of Sample Building

The building used in the study, is a two-storey residential (villa) building and has a total floor area of 217,80 m². The architectural ground floor plan and an elevation plan of the building are given in Figure 3 and Figure 4, respectively.

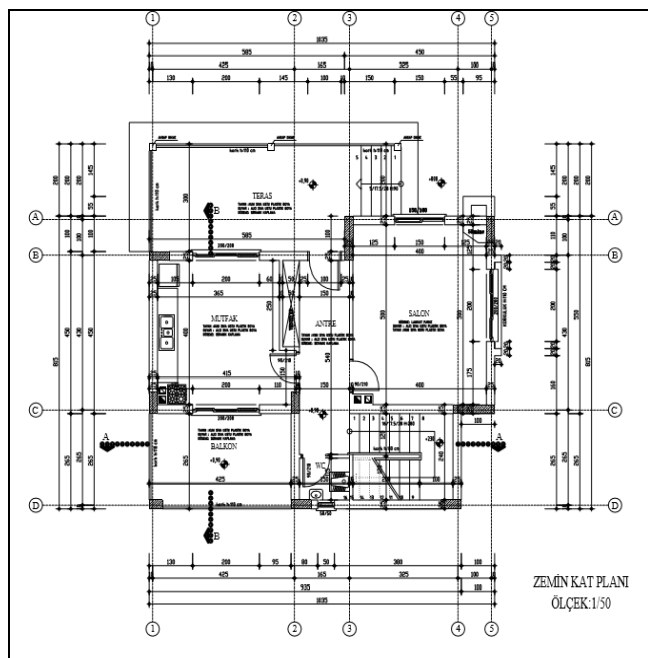


Figure 3. Architectural ground floor plan.

3.2 Static Analysis and Assessment (Results)

In this study, static analysis of the structures, designed according to the different soil classes, were performed by using Sta4-CAD [14] which is the most used structural analysis program in Turkish project market. It's assumed that all buildings are located in the 1st degree seismic zone as shown in Fig.2, and are designed according to different local soil classes. The effective ground acceleration coefficient was taken as 0.40 in the 1st degree earthquake zone as specified in the Turkish Seismic Design Code (TSDC 2018).

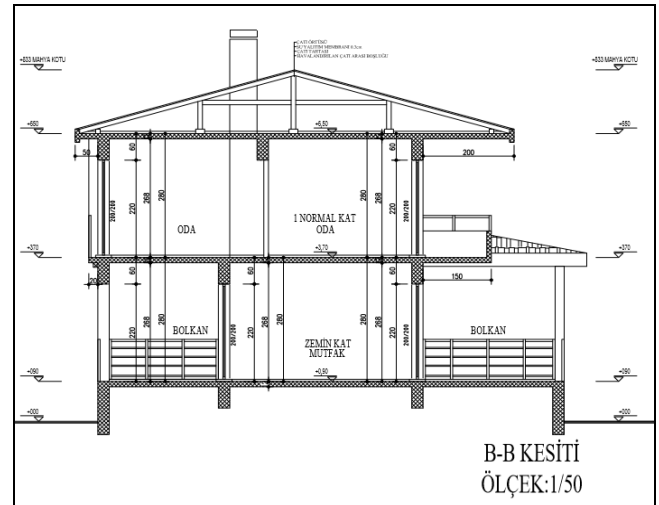


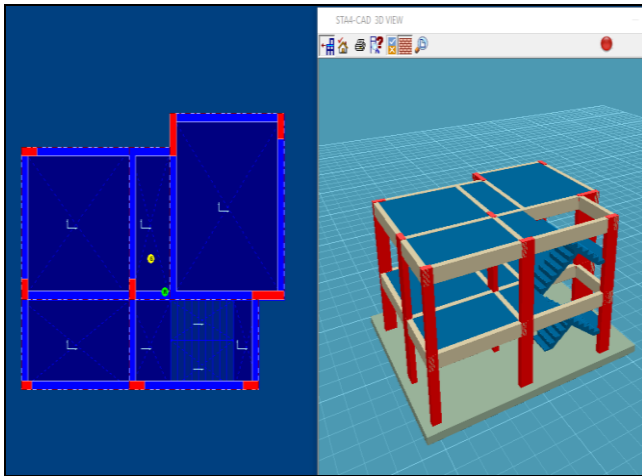
Figure 4. Architectural cross-section for building.

Seismic ground response characteristic periods (T_a and T_b) according to the defined soil categories (ZA-ZD) and soil classes (Z1-Z4) are presented in Table 3.

Table 3. Spectrum characteristic parameters according to the soil classes in TSC 2007.

| Soil Group | Local Site Class | I (Building Importance Factor) | A_0 (Effective Ground Acceleration Coefficient) | Safe/allowable Stress (Mpa) | Subgrade Reaction Coefficient (KN/m ³) | T_a | T_b |
|------------|------------------|--------------------------------|---|-----------------------------|--|-------|-------|
| ZA | Z1 | 1 | 0,4 | 0,39 | 5000 | 0,10 | 0,30 |
| ZB | Z2 | 1 | 0,4 | 0,29 | 3000 | 0,15 | 0,40 |
| ZC | Z3 | 1 | 0,4 | 0,20 | 2000 | 0,15 | 0,60 |
| ZD | Z4 | 1 | 0,4 | 0,15 | 1000 | 0,20 | 0,90 |

The three dimensional building model and its raft foundation are given in Figure 5. Figure 6 and Figure 7 shows the column application and formwork plans which are created as a result of static analysis.



a) Floor Plan of Reinforced Concrete (RC) Building
b) 3D view of Reinforced Concrete (RC) Building

Figure 5. Finite element modeling of reinforced concrete building.

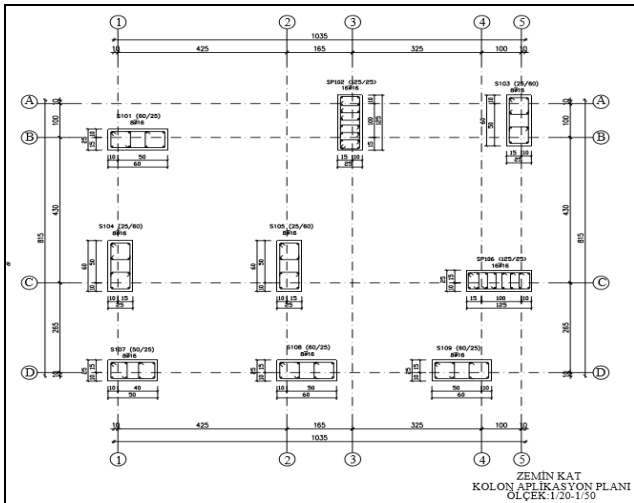


Figure 6. showing different kinds of columns reinforcement.

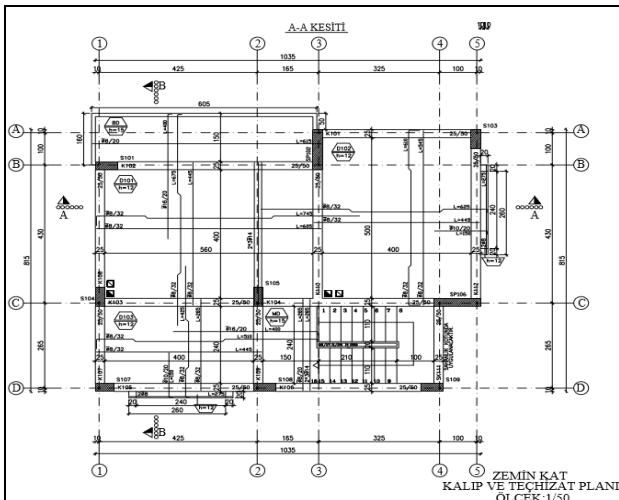


Figure 7. First floor slab reinforcement plan view.

The difference in the local soil classes resulted in different dimensions of the concrete column and the dimensions of the foundation thickness. As a result of analysis performed, the specified maximum soil stresses are shown in Figure 8.

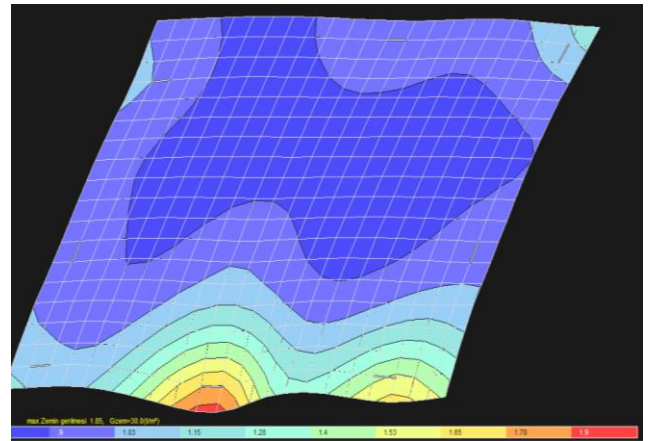


Figure 8. Stress distribution in soil.

Each of the colors resulting from analyzes corresponds to a safe/allowable stress range. The values of the soil safe/allowable stresses corresponding to these colors are given in Table 4.

Table 4. Stress Scale and Stress Distribution Values.

| Colors | Corresponding Soil Safe/allowable Stress Scale (Mpa) |
|---------------|--|
| Red | ≥ 0.019 |
| Orange | 0.018-0.019 |
| Yellow | 0.016-0.018 |
| Light-yellow | 0.015-0.016 |
| Green | 0.014-0.015 |
| Turquoise | 0.013-0.014 |
| Blue | 0.012-0.013 |
| Dark blue | 0.010-0.012 |
| Navy blue | 0.009-0.010 |
| Prussian blue | ≤ 0.009 |

The steel reinforcement, concrete and formwork obtained from the results of the analysis, which is performed considering different local soil classes. At the same time, it's concluded that different local soil classes cause changes in the building costs.

4. RESULTS

For different local soil classifications, the concrete, steel reinforcement and formwork of the projects are obtained from the results of static analysis. The estimation of quantity cost is calculated by multiplying with the 2017 unit costs specified by the Ministry of Environment and Urbanization and construction costs were calculated and the results of the calculations are given in Table 5 [3].

Table 5. Estimation of Quantity and Cost for Different Local Site Classes.

| 1st Degree Earthquake Zone | | | | | | | | |
|----------------------------|--------------------|----------------|-------|----------------------------|---------------------|---------|----------------------------|-------|
| Soil Group | Local Site Classes | Quantity | | | Unit Cost | | | Total |
| | | Concrete | Rebar | Structural Member Formwork | Concrete | Rebar | Structural Member Formwork | |
| | | m ³ | kg | m ² | m ³ / TL | kg / TL | m ² / TL | |
| ZA | Z1 | 70.03 | 6980 | 323.06 | 188 | 3650000 | 38 | 50919 |
| ZB | Z2 | 71.5 | 7910 | 325.6 | 188 | 3650000 | 38 | 54686 |
| ZC | Z3 | 76.8 | 8470 | 328 | 188 | 3650000 | 38 | 57818 |
| ZD | Z4 | 79.06 | 9580 | 331.1 | 188 | 3650000 | 38 | 62412 |

The official unit costs determined by the Ministry of Environment and Urbanization have been used with the idea that there will be price difference in the regional and brand changes of the materials. In the reinforcing pricing, the code number 23.014-15 St III is used, for the timber formwork, the code number 21.011-TAK is used for minimum unit price and in concrete pricing; the maximum unit price was taken as 16.058 / 1.

As a result of the work done, it has been observed that there is a 22.57% cost difference in the construction costs of the buildings in ZA and ZD local soil classes. By observing Fig.9 it is apparent that different soil classes cause changes in the building costs. A comparison of analysis of costs is given in Figure 9.

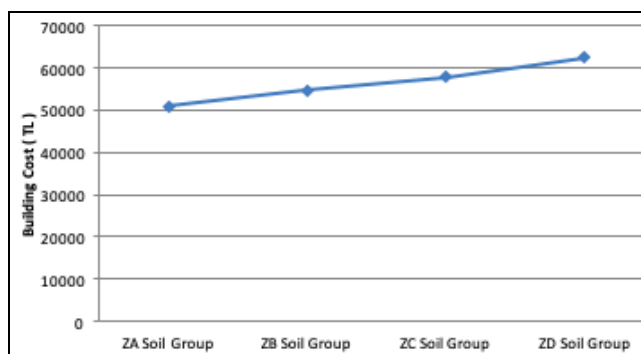


Figure 9. Construction Cost Graph of Structures of Different Local Site Classes.

5. CONCLUSION

In the present study, within the scope of 2018 Turkish seismic building code, the effects of local soil conditions on the seismic response of buildings and the resulting changes in building cost examined with the example structure. As because of the finite element method based software used in this study which is Sta4-Cad is not compatible with the new developed 2018 Turkish seismic building code in regards of soil parameters or etc., in the analysis phases some assumptions must be done and this comes through as a limitation of the study. It has been observed that there is a 22.57% cost difference in the construction costs of the buildings in ZA and ZD local soil classes. As seen from the results, the different type of soil classifications will have significant impacts on the cost of construction of the buildings.

It can be concluded that when designing new structures or assessing the existing structures, corresponding the local soil conditions should be accounted for using the spectral acceleration coefficients in 2018 TBEC.

REFERENCES

- [1] Burhan C. Işık, 1992. Depremler ve Türkiye, Yıldız Teknik Üniversitesi-İstanbul.
- [2] H. Çanakçı, and M. Gögüs, 2001. "Yerel Zemin Sınıfının Hatalı Belirlenmesinin Yapıya Gelen Yatay Yüklere Etkisi," Türkiye İnşaat Mühendisliği XVI. Teknik Kongre ve Sergisi Yüklere Etkisi, Teknik Kongre ve Sergisi, Ankara.
- [3] Çevre ve Şehircilik Bakanlığı 2017 birim fiyat listesi, http://www.csb.gov.tr/db/donersermaye/editordosya/2017_Yili_Birim_Fiyat_Yeni_20_11_2017.pdf
- [4] Z. Çelep, and N. Kumbasar, 2000. "Deprem Mühendisliğine Giriş ve Depreme Dayanıklı Yapı Tasarımı," Sf. 596, İstanbul.
- [5] B. Yön, M. E. Öncü, and Y. Çalayır, 2014. "Effects of seismic zones and site conditions on response of RC buildings," *Gradevinar* 67 (6), Sf. 585-596.
- [6] Ö. Muratoğlu, and Ö. Özkan, 2005. "Zemin Sınıfları ve Deprem Bölgelerinin Bina Yatay Yüklere Etkisi," *Deprem Sempozyumu, Bildiriler Kitabı*, Sf. 1097-1104, 2001.
- [7] TMMOB Afet Sempozyumu, Bildiriler Kitabı, 5-7 Aralık 2007 - Ankara.
- [8] Afet İşleri Genel Müdürlüğü.(Webpage – Database, December, 2018)
- [9] Deprem Etkisi Altında Binaların Tasarımı İçin Esaslar, Yönetmelik, 2018.
- [10] Afet İşleri Genel Müdürlüğü Deprem Araştırma Dairesi. (Webpage - Database)
- [11] B. Yön, M. E. Öncü, and Y. Çalayır, 2014. "Effects of seismic zones and site conditions on response of RC buildings," *Gradevinar* 67 (6), Sf. 585-596.
- [12] E. Işık, A. Büyüksaraç, and M.C. Aydın, 2016. "Effects of local soil conditions on earthquake damages," The 2nd CEPPIS International Scientific Conference on Civil Engineering: Present Problems, Innovative Solutions (CEPPIS).
- [13] I. Okawa, T. Kashima, S. Koyama, and Y. Kitagawa, Sunday 30 January - Friday 4 February 2000. "An Evaluation of Surface Soil Amplification Properties from the Analysis of Recorded Motions," 12th World Conference on Earthquake Engineering, Auckland, New Zealand.
- [14] STA4CAD 2010: Analysis and design manual of multi-storey RC structures, V13.1 STA Computer Engineering and Consulting Company, Istanbul, Turkey.

The Experiment and Simulation Results of Speed Control of Permanent Magnet Synchronous Motor by Using Fuzzy Controller

Aykut Teker¹ and F. Erfan Kuyumcu²

¹Siemens Sanayi ve Ticaret Anonim Sirketi, Yakacik Caddesi No:111, 34870
Istanbul, Turkey
aykut.teker@siemens.com

²Istanbul Gedik University, Engineering Faculty, Electrical-Electronic Engineering Department,
Kartal, Turkey
feriha.kuyumcu@gedik.edu.tr

Received: 28.11.2018 Accepted: 25.12.2018

Abstract – This paper is concerned with the topics on the speed control of Permanent Magnet Synchronous Motor (PMSM) with using Matlab/Simulink in real system. The speed control of motor model is done with Fuzzy Logic controller. The Simulation and experimental results of controller performances are compared with the speed graphs obtained.

Keywords: Fuzzy control, permanent magnet synchronous motor, simulation, experimental, application.

1. INTRODUCTION

The PM Synchronous motors are being increasingly used in a wide range of applications because of their high power density and efficiency. In the classical control, most of the automatic control problems are usually solved by mathematical tools based on the system model but in the real world, there are many complexes industrial processes whose real models can't be easily developed. Hence, a fuzzy logic controller using linguistic information applies to the model the qualitative aspects of human knowledge, providing an alternative to conventional control techniques [2].

In this paper, fuzzy control is used for speed control of PM synchronous motor. Experiment and simulation results of controller performances are compared with graphs obtained. For speed control method, a fuzzy logic using error and derivative of error inputs is proposed. The basis of the development of the fuzzy logic controller is the analysis of the PMSM transient response and fuzzy logic. The fuzzy controller generates the variations of the reference current vector of the PMSM speed control based on the speed error and its change. The results of experiment and simulation show that the fuzzy controller can be used in sensitive application. This application of fuzzy logic to automation and control engineering represents a logical extension of traditional control technology [1].

2. MATHEMATIC MODEL OF PMSM BY MATLAB / SIMULINK

The stator of the PMSM and the wound rotor synchronous motor (SM) are similar. In addition there is no

difference between the back electromotive force (emf) produced by a permanent magnet and that produced by an excited coil. Hence the mathematical model of a PMSM is similar to that of the wound rotor SM. The following assumptions are made in the derivation: Saturation is neglected although it can be taken into account by parameter changes, the back EMF is sinusoidal, eddy currents and hysteresis losses are negligible. The parameters of PM Synchronous Motor are given in the Table I.

Table 1. Parameters of PM Synchronous Motor.

| Parameter | Description | Value |
|-------------|--------------------------------------|----------------------|
| R_s | Stator phase resistance (Ω) | 10.4 |
| p | Number of poles per phase | 4 |
| L_d | Inductance (mH) d-axis | 43 |
| L_q | Inductance (mH) q-axis | 43 |
| λ_m | Magnetic Flux Linkage (Wb) | 0.1 |
| J | Inertia (kgm) | $0.94 \cdot 10^{-4}$ |
| B | Flux Density (Nmsrad) | ≈ 0 |

Motor model is constituted of following equations:

$$T_e = \frac{3}{2} \cdot \frac{p}{2} [\lambda_m i_q + (L_d - L_q) i_d i_q] \quad (1)$$

$$\frac{d(i_d)}{dt} = \frac{V_d - R_s i_d + \omega_r L_q i_q}{L_d} \quad (2)$$

$$\frac{d(i_q)}{dt} = \frac{V_q - R_s i_q + \omega_r L_d i_d + \lambda_m}{L_q} \quad (3)$$

$$\frac{d(\omega_{rm})}{dt} = \frac{T_e - T_L - B\omega_{rm}}{J} \quad (4)$$

Where T_L is the load torque, B is the viscous frictions, J is the moment of inertia, V_d and V_q represent the d-q axes stator voltages, i_d and i_q are d-q axis stator inductances, R_s is the per phase stator resistance, ω_r shows the electrical velocity of the rotor. λ_m is expression of the flux linkage due to the rotor magnets linking the stator, T_e is the motor produced torque and ω_{rm} is the mechanical velocity of the rotor. For this study, real parameters of machine are used as given Table I. The results of this simulation can be compared with the results of the real experiment.

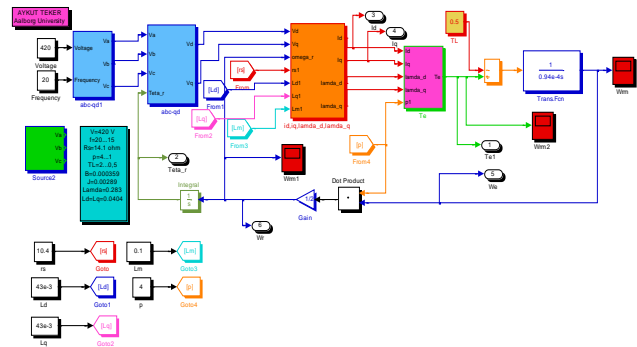


Figure 1. Mathematics model of PMSM.

2.1. Control Strategies

The PM Synchronous motor is a rotating electric machine where the stator is a classic three phase stator as an induction motor and the rotor has surface-mounted permanent magnets. In this respect, the PMSM is equivalent to an induction motor in which the air gap magnetic field is produced by a permanent magnet. The use of a permanent magnet to generate a substantial air gap magnetic flux makes it possible to design highly efficient PM motors.

The rotor speed ω_r is compared with the reference speed ω_r^* and the resulting error is processed in the fuzzy speed controller for each sampling interval. For low speed operation of PM motors the flux weakening effect is not required, however the effect of flux weakening is observed for the high speed operation of PMSM. Hence in this analysis, the direct axis reference current i_d^* is considered to be zero for low speed operation.

The d-q axis reference currents i_d^* are used to generate the reference currents i_a^* , i_b^* and i_c^* in the reference current generator. The reference currents have the shape of sinusoidal wave in phase with respective back emf to

develop a constant and unidirectional torque. In PWM current regulating block, the motor winding currents are compared with the reference currents and the switching commands are generated for the inverter devices. In the case of sinusoidal fed PM motor, the orientation of the stator current gives a highly desirable characteristic. By neglecting the flux weakening effect for the low speed operation of the motor, the reference direct axis current (i_d^*) becomes zero.

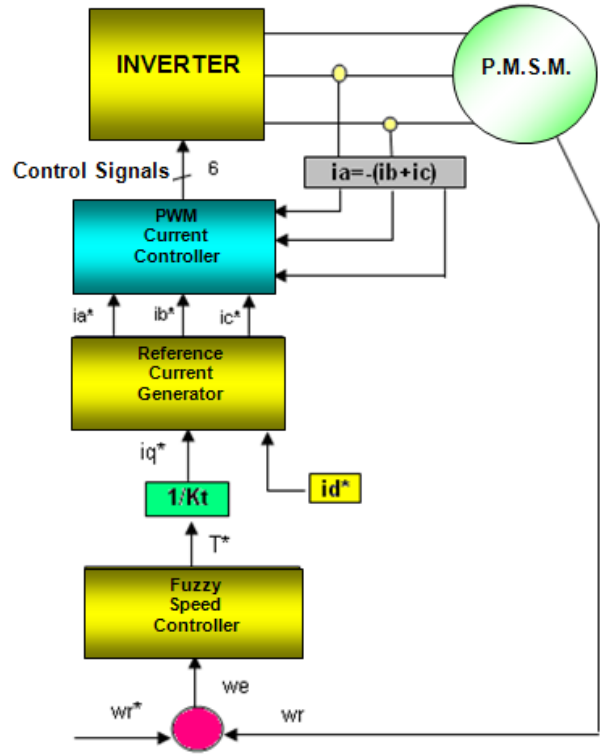


Figure 2. Schematic block diagram of Fuzzy controlled PMSM drive.

2.2. Fuzzy Controller Structure

The kind of a structure that a fuzzy controller will have will primarily depend on the controlled process and demanded quality of control. Since the application area for fuzzy control has widely use, there are many possible controller structures, some differing significantly from each other by the number of inputs and outputs, or less significantly by the number of input and output fuzzy sets and their membership functions forms, or by the form of control rules, the type of inference engine, and the method of defuzzification [3].

All that variety is the designer's disposal, and it is up to the designer to decide which controller structure is optimal for a particular control problem. The basic structure of a fuzzy controller is shown in Figure 3. Although there are many analog fuzzy controllers on the market, most of today's fuzzy controllers are implemented in digital form. This is the reason why the term B/F conversion is introduced here as inputs of a digital fuzzy controller are defined over discrete universes of discourse with the finite number of elements (integers) obtained after quantization of sensor signals. Fuzzy controller has a disadvantage. The amount of rule base of the fuzzy controller is bigger when the sensitivity of the output is high, and how to reduce memory capacity is crucial [1].

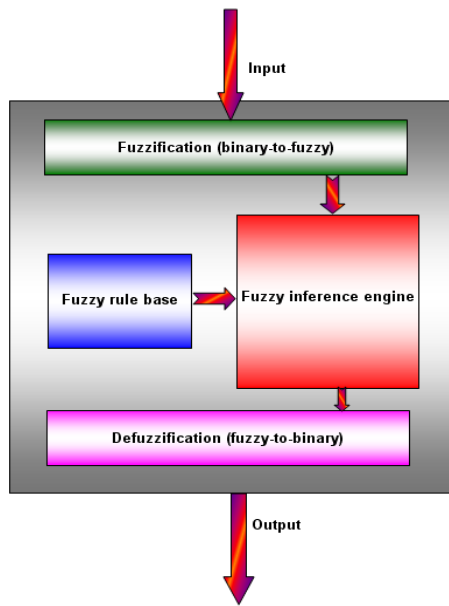


Figure 3. The structure of a fuzzy logic controller.

Fuzzy Logic controller executes the 49 control rules shown in Table 2 taking the fuzzy variables “e” and “de” as inputs and output quantity. The rules are formulated by using the knowledge of the PM synchronous motor behavior and the experience of control engineers.

3. COMPARATIVE SIMULATION AND EXPERIMENT RESULTS

The usage of simulation software packages for modeling, simulation, and optimization of control systems has become a part of regular engineering practice. Recently added features of such software packages like a possibility to generate real-time executable code directly from simulation models enabled shorter development times and faster validation of new control solutions. The solutions developed with the world standard software packages like Matlab, Matrix, or Mathematical, are available to a large number of users [1].

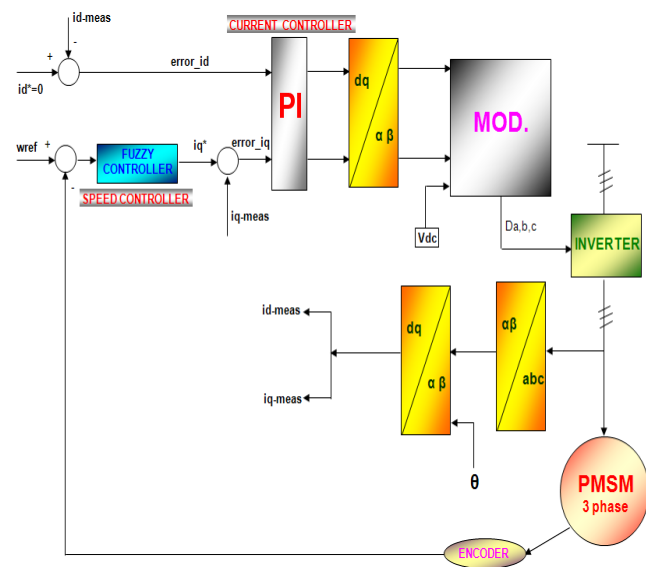


Figure 4. Control block of PMSM.

Since Matlab contains the Fuzzy Logic Toolbox (FLT) that allows the designer to create and test new fuzzy control designs, we give a short description of basic features of the Matlab Fuzzy Logic Toolbox needed for the successful usage of the tool.

For low speed operation of PM motors the flux weakening effect is not required, however the effect of flux weakening is deserved for the high speed operation of PMSM. Hence in this analysis, the direct axis reference current i_{dref} is considered to be zero for low speed operation. The d-q axis reference currents i_{dref} and i_{qref} are used to generate the reference currents i_{aref} , i_{bref} and i_{cref} in the reference current generator.

The reference currents have the shape of sinusoidal wave in phase with respective back emf to develop a constant and unidirectional torque. In PWM current regulating block, the motor winding currents are compared with the reference currents and the switching commands are generated for the inverter devices.

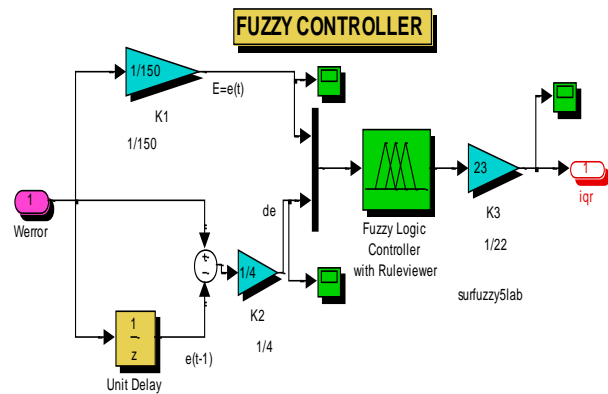


Figure 5. Fuzzy block for PMSM.

The goal of designed FLC in this study is to minimize speed error. The larger speed error the bigger controller input is expected. In addition, the change of error plays an important role in define controller input. Consequently FLC uses error $e(t)$ and change of error $de(t)$ for linguistic variables which are generated from the control rules. Equations determine required system equations. The output variable is the change in control variable $du(t)$ of motor driver. Here K_1 , K_2 , and K_3 are each gain coefficients and t is a time index.

$$e(t) = [\omega_{ref}(t) - \omega(t)]K_1 \tag{5}$$

$$de(t) = [e(t) - e(t-1)]K_2 \tag{6}$$

$$du(t) = [u(t) - u(t-1)]K_3 \tag{7}$$

The error (e) approaches to its smallest value when the motor speed is attained to nominal value. If we reverse this value, the error interval can be defined between -60 and 60. In order to optimize the speed control, the intervals of membership functions are found after some manual changes as follow:

e_w : -150 and +150 rad/s
 de_w : -4 and +4 rad/s/s
 u : 23 and -23

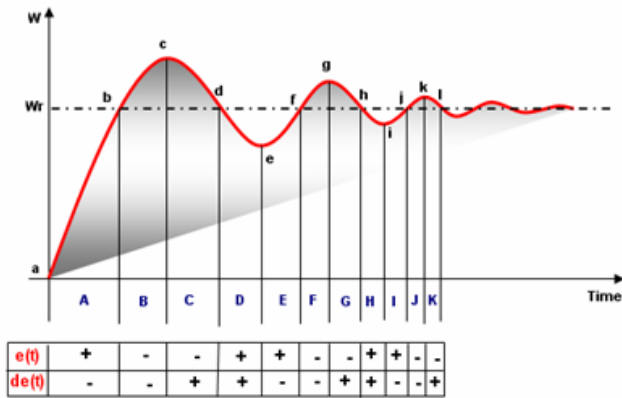


Figure 6. Output for rule table.

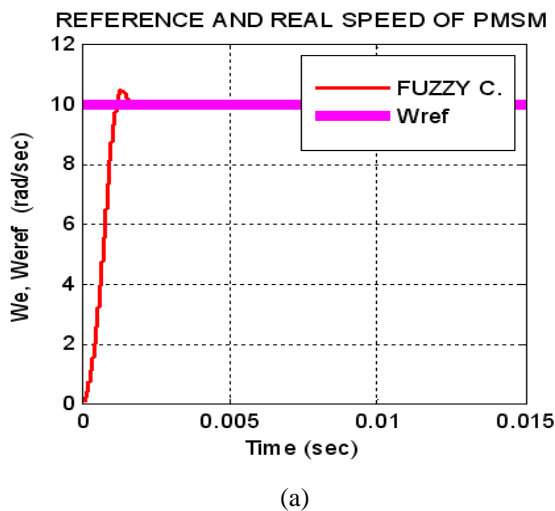
The gain values are determined for these intervals in simulation model as $K_{1e}=1/150$, $K_{2de}=1/4$ and $K_{3u}=23$.

System speed comes to reference value by means of the defined rules. For example, first rule on Table II determines, 'If ($e(t)$ is NB) and ($de(t)$ is NB) then ($u(t)$ is NB)'. According to this rule, if error value is negative big and change of error value is negative big then output will negative big.

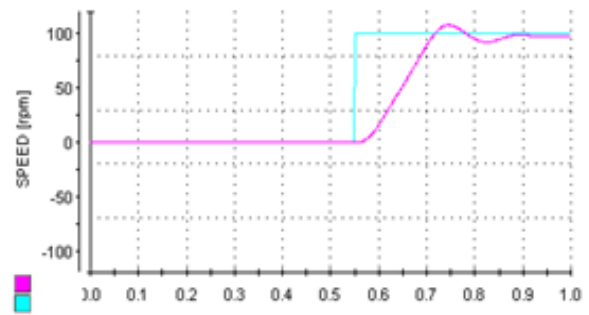
Table 2. Rule Table For Fuzzy Controller.

| $de(t)$ $e(t)$ | NB | NM | NS | ZERO | PS | PM | PB |
|-------------------|----|----|----|------|----|----|----|
| NB | NB | NB | NB | NM | NS | PM | PS |
| NM | NB | NB | NB | NB | NM | NM | PB |
| NS | NB | NB | NM | NS | PS | PS | PM |
| ZERO | NB | NM | NS | ZERO | PS | PM | PB |
| PS | NM | NS | NS | PS | PM | PM | PB |
| PM | NS | NM | PS | PM | PB | PB | PB |
| PB | NB | PS | PM | PB | PB | PB | PB |

The user can decide to these rules with their experiment. For example, B interval in Figure 6, motor speed is larger than reference speed and still wants an increase strongly. This state corresponds to decrease motor voltage decreasing. All conditions in the control process are shown in Figure 6.



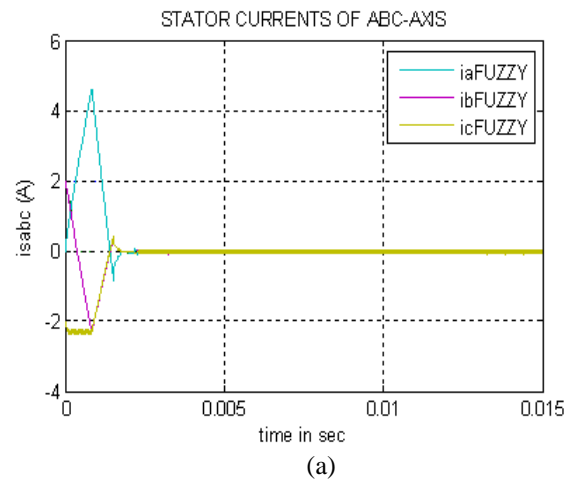
(a)



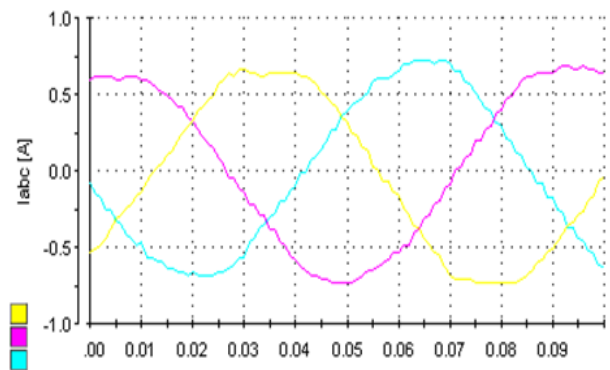
(b)

Figure 7. a) Simulation results, b) Experimental results for speed.

Figure 7 shows the motor starting response in which it takes around 0.0015 seconds for fuzzy to reach the set reference speed. This figure shows simulation results of Fuzzy controller and experiment results for Fuzzy controller.



(a)



(b)

Figure 8. a) Simulation results, b) Experimental results for i_{abc} .

DSPACE program what is used for connection from computer to motor in real system. 25 rules are used at fuzzy in real system for controlling because the data communication of fuzzy in Matlab is faster than DSPACE.

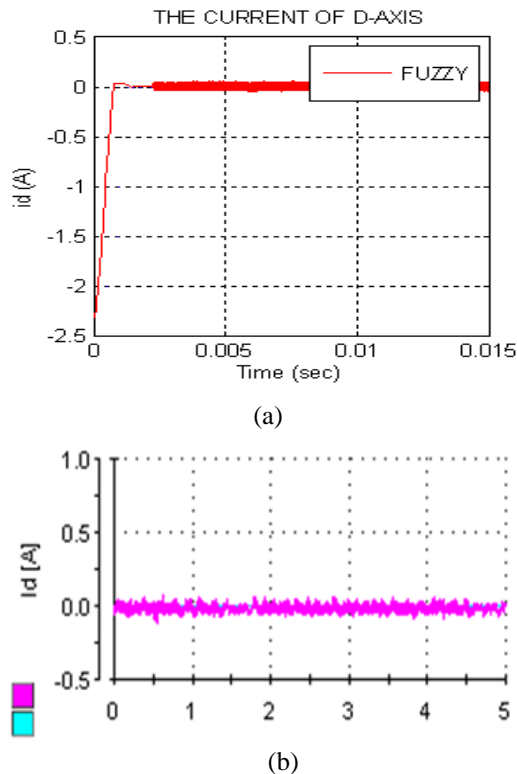


Figure 9. a) Simulation results, b) Experimental results for i_d .

The speed reaches to reference speed very fast by fuzzy. The overshoot can be regulated by Fuzzy. Figure 8 shows stator currents of abc-axis of PMSM.

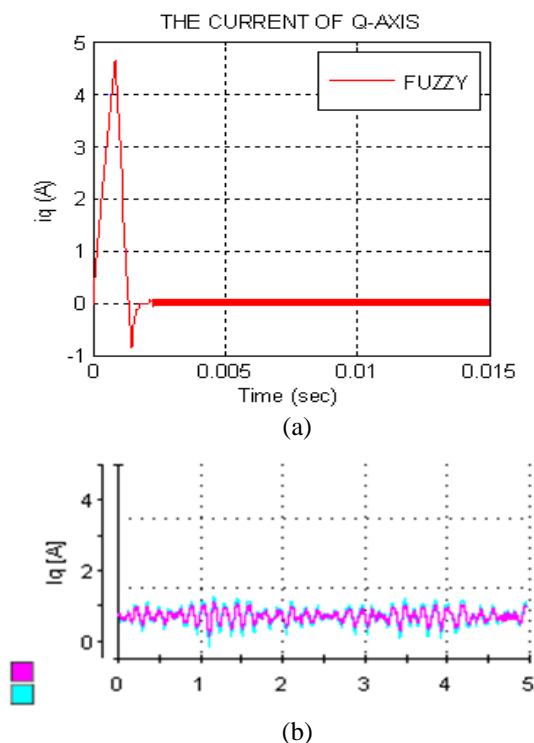


Figure 10. a) Simulation results, b) Experimental results for i_q .

Figure 9 shows flux linkage of d-axis of PMSM. The figure shows that i_d current is zero. It means that experimental works are true. Figure 10 shows flux linkage of q-axis of PMSM. This current is changed by torque.

4. CONCLUSION

PMSM speed control has been performed in Matlab Simulink environment. PMSM speed has been controlled with Fuzzy Logic Controller (FLC). In this study, it is also designed a circuit model as a driver to get more reasonable results. This paper shows that simulation of Fuzzy Logic Controller has clearly better performance for providing T_r (rising time), e_{ss} (steady state error) and t_r^* (rising time to reference speed) $\%M_p$ (percent overshoot) criteria in comparison to the experimental results. FLC also has more sensitive responses against load disturbances in according to classical PID controller.

Table 3. Experimental And Simulation Results For Fuzzy Controller.

| | Simulation Results | Experimental Results | Discrepancy | Signal |
|--------------|--------------------|----------------------|-------------|--------|
| t_r (s) | 0.00125 | 0.08 | 0.07875 | (-) |
| e_{ss} (s) | 0.0015 | 0.3 | 0.2985 | (-) |
| M_p (%) | 3 | 3 | 0 | (+) |
| t_r^* (s) | 0.0013 | 0.1 | 0.0987 | (+) |

The fuzzy controller can be used at sensitive applications. PMSM has been used widely in the control system of high performance depending development of the power electronic and control technology. However, the performances of the PMSM are very sensitive to the parameter and load variations.

Finally the fuzzy controller generates the variations of the reference current vector of the PMSM speed control based on the speed error and its change. The fuzzy controller is better than classical control because this control method can be regarded as an adaptive control based on a linguistic process. The linguistic process is however is based on prior experience and heuristic rules used by human operators.

ACKNOWLEDGEMENTS

The authors would like to thank Associate Professor Ewen RITCHIE, Aalborg University in Denmark for his contributions of knowledge and good ideas to this project and also would like to thank Lu KAIYUAN and Gaizka ALMANDOZ for their help at laboratory in Denmark too.

REFERENCES

- [1] C.-F. J. Kuo, C.-H. Hsu, C.-C. Tsai, Control of a Permanent Magnet Synchronous Motor With a Fuzzy Sliding-Mode Controller, *Springer-Verlag London Limited* 2006, DOI 10.1007/s00170-005-0393-2.
- [2] M.K. Rahmat, S. Jovanovic, K.L. Lo, Reliability and Availability Modelling of Uninterruptible Power Supply Systems Using Monte-Carlo Simulation, *International Review of Electrical Engineering (IREE)*, vol. 1 n. 3, August 2006, pp. 374 – 380.
- [3] J.R. Hendershot, T.J. Miller, *Design of Brushless Permanent-Magnet Motors*, (UK, 1994).
- [4] Harris, J., *Fuzzy Logic Applications in Engineering Science*, National University of Science and Technology, Zimbabwe, (Springer, ISBN-13 978-1-4020-4078-8).



Istanbul
GEDİK
University
2651-5199